

How Robust are the Inferred Density and Metallicity of the Circumgalactic Medium?

Anshuman Acharya^{1,2*} and Vikram Khaire^{3,4}

¹Indian Institute of Science Education and Research (IISER) - Mohali, SAS Nagar, Punjab - 140306, INDIA

²Max Planck Institut für Astrophysik, Garching - 85748, Germany

³Indian Institute of Space Science & Technology, Thiruvananthapuram, Kerala - 695547, INDIA

⁴Physics Department, Broida Hall, University of California Santa Barbara, Santa Barbara, CA 93106-9530, USA

ABSTRACT

Quantitative estimates of the basic properties of the circumgalactic medium (CGM), such as its density and metallicity, depend on the spectrum of incident UV background radiation. Models of UV background are known to have large variations, mainly because they are synthesized using poorly constrained parameters, which introduce uncertainty in the inferred properties of the CGM. Here, we quantify this uncertainty using a large set of new UV background models with physically motivated toy models of metal-enriched CGM. We find that, the inferred density and metallicity of low-density (10^{-5} cm^{-3}) gas is uncertain by factors of 6.3 and 3.2, whereas high density (10^{-3} cm^{-3}) gas by factors of 4 and 1.6, respectively. The variation in the shape of the UV background models is entirely responsible for such a variation in the metallicity while variation in the density arises from both normalization and shape of the UV background. Moreover, we find a harder (softer) UV background infers higher (lower) density and metallicity. We also study warm-hot gas at $T = 10^{5.5} \text{ K}$ and find that metallicity is robustly estimated but the inferred density is uncertain by a factor of 3 to 5.4 for low to high-density gas. Such large uncertainties in density and metallicity may severely limit the studies of the CGM and demand better observational constraints on the input parameters used in synthesizing UV background.

Key words: quasars: general < Galaxies, galaxies: haloes < Galaxies, galaxies: evolution < Galaxies, intergalactic medium < Galaxies

1 INTRODUCTION

Galaxies form, feed, and grow by accreting pristine gas from the intergalactic medium (IGM) and spew metal-enriched gas into vast distances. Much of this active trade of gas determines the evolution of galaxies. The region where this trade happens is located around galaxies at the interface between their discs and the IGM, known as the circumgalactic medium (CGM). Therefore, studying the gas in the CGM, its distribution, chemical composition and physical conditions around different types of galaxies may play a crucial role in understanding the galaxy formation and evolution (see review; Tumlinson et al. 2017).

In recent times, much of the insights on the CGM around different galaxies have been obtained from promising large observational campaigns (e.g., Stocke et al. 2013a; Tumlinson et al. 2013; Bordoloi et al. 2014; Burchett et al. 2019; Chen et al. 2020) and dedicated efforts to simulate the small scale structure of the CGM (e.g., Hummels et al. 2013, 2019; Churchill et al. 2015; Nelson et al. 2020;

Oppenheimer et al. 2018; van de Voort et al. 2019; Peebles et al. 2019). There is an important ingredient needed for both, simulating the CGM as well as gaining insights from observations, known as the ionizing UV background radiation. For the absorption-line studies of CGM absorbers, this all-prevailing spectrum of the UV background is needed for determining the physical conditions and chemical composition of the CGM gas. This is achieved by relating the observed ionic abundances to the total abundances of gas by performing an ionization correction. The results of which determine the density and metallicity of gas which can be used to quantify the mass and line-of-sight size of the CGM absorbers and their total metal content (e.g., Stocke et al. 2013b; Shull et al. 2014; Prochaska et al. 2017; Mohapatra et al. 2019, 2021). Moreover, the spectrum of the UV background is essential to determine if the absorbing gas is single-phase or multi-phase (e.g., Tripp et al. 2008; Narayanan et al. 2009; Savage et al. 2014; Sameer et al. 2021), photoionized or collisionally ionized (e.g., Hussain et al. 2015, 2017; Pachat et al. 2017; Haislmaier et al. 2020), or if it shows any enhancement in the relative abundances of the metals compared to the solar abundances (e.g., Pettini et al. 2008; Cooke et al. 2011; Shull et al.

* E-mail: anshuman@mpa-garching.mpg.de

2014). Mostly, individual CGM studies assume a single model of the UV background in their analysis and it is not always feasible, or generally expected, to use a range of all possible UV background models.

Because direct observations of the UV background are not possible, it needs to be synthesized via a cosmological radiative transfer of UV photons emitted by quasars and galaxies through the IGM (see [Miralda-Escude & Ostriker 1990](#); [Haardt & Madau 1996](#); [Shull et al. 1999](#)). Therefore, the spectrum of the synthesized UV background depends on the UV emissivity of quasars and galaxies, the distribution of gas in the IGM and also on various assumptions that are part of the modeling (for more details see section 4.4 of [Khaire & Srianand 2019](#)). In particular, it is more susceptible to the poorly constrained emissivities of quasars and galaxies and shows large variation at any redshift even among the latest models (see Fig. 1) obtained using the most updated observations of inputs ([Khaire & Srianand 2019](#); [Puchwein et al. 2019](#); [Faucher-Giguère 2020](#)). Such a variation in the UV background models can lead to a varying degree of inferred properties of the CGM absorbers and reported results depend on the choice of UV background models. This was illustrated previously by [Hussain et al. \(2017\)](#) for the case of Ne VIII absorbers and [Chen et al. \(2017\)](#) for metallicity estimates. Given the large uncertainty in the UV background models, it is important to know how much variation (or a systematic uncertainty) one expects in the inferred basic properties of the CGM gas, such as its density and metallicity. Past research using older UV background models like [Haardt & Madau \(2012\)](#) and [Faucher-Giguère et al. \(2009\)](#) have noted systematic uncertainties in metallicity like in [Lehner et al. \(2013\)](#) and more recently [Wotta et al. \(2019\)](#) for cool, photoionized gas. In this paper, we quantify these variations with the help of widely used `CLOUDY` software ([Ferland et al. 1998, 2017](#)) for ionization modelling and a set of nine latest UV background models. We use seven viable UV background models as described in [Khaire & Srianand \(2019\)](#) (hereafter **KS19**) where the spectral energy distribution (SED) of quasars was varied to obtain the quasar emissivity in the UV background models. Such a variation is within the reported observational range and also consistent with high- z observations of He II (see [Khaire 2017](#)).

In addition to these seven models, we also use two more latest UV background models; [Puchwein et al. \(2019\)](#) (hereafter **P19**) and [Faucher-Giguère \(2020\)](#) (hereafter **FG20**), which are updated versions of previous UV background models by [Haardt & Madau \(2012\)](#) and [Faucher-Giguère et al. \(2009\)](#), respectively. For illustrating the differences, we show all these nine UV background models at $z = 0.2$ in Fig. 1 and discuss the details in Section 2.

Using `CLOUDY` (v17.02; [Ferland et al. 2017](#)), we irradiate a gas cloud with a preferred UV background model and create mock CGM observations. We use two types of `CLOUDY` models for creating mock observations, in first type of models, the absorber is kept in thermal and photoionization equilibrium with the UV background, while in second type the absorber is a warm-hot gas having high temperatures ($T = 10^{5.5}$ K). We note down the output column densities of many metal ions from these models and treat a subset of those as our mock CGM observations. These mock observations are then used to infer the density and metallicity of the absorbing gas with different UV background models. Difference between the inferred values of density and metallicity for a UV background model and the true values (that are used for generating mock observations with a preferred UV background), quantifies the expected variation arising from using different UV background models.

We find that, by varying the UV background models the inferred density and metallicity of low-density (10^{-5} cm $^{-3}$) gas can be

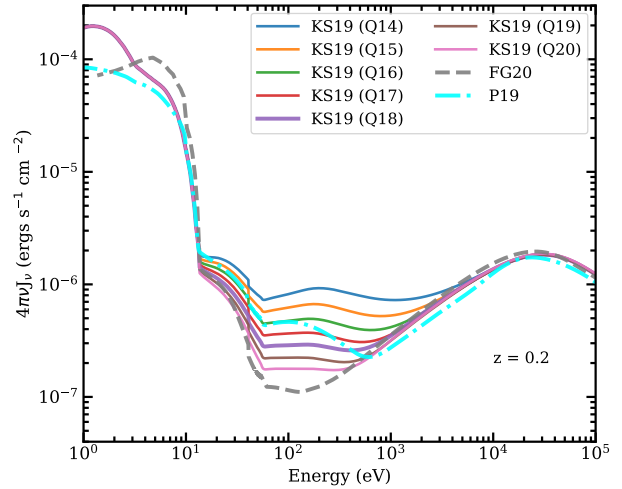


Figure 1. The UV background spectrum at $z = 0.2$. Solid lines show **KS19** UV background models obtained by varying intrinsic quasar SED (a power-law $L_\nu \propto \nu^{-\alpha}$) index α from 1.4 (model Q14) to 2.0 (model Q20). We also show two new UV background models by **P19** and **FG20**. Even though all of these models show large variation, they are the most updated versions of the UV background and all of them are physically viable (see Fig. 2).

off by factors of 6.3 and 3.2, whereas high density (10^{-3} cm $^{-3}$) gas can be off by factors of 4 and 1.6, respectively. For warm-hot absorber at $T = 10^{5.5}$ K, we find that metallicity is robustly estimated but the inferred density can be off by a factor of 3 to 5.4 for low to high-density gas. In addition to this, we also discuss the relative effect of shape and normalization of UV background models on the inferred densities and metallicities.

The paper is organized as follows. In Section 2, we briefly discuss the UV background models used in the study. In Section 3, we explain our mock CGM observations and present the method to infer the density and metallicity of the CGM gas from those. In section 4 we present our results for the different UV background models, and quantify the variation in the inferred density and metallicity for both photoionized and warm-hot absorbers. In section 5 we summarize main results of the paper.

2 THE UV BACKGROUND MODELS

We use seven UV background models from **KS19** and two recent additional models from **P19** and **FG20**. In Fig. 1, we show the predictions of these nine models at $z = 0.2$. There is a large variation in the model intensity of UV background at energy range $10 - 10^3$ eV, notably almost an order of magnitude around $50 - 500$ eV. Ionization potentials of most of the metal ions that are typically observed in the CGM fall in the energy range $\sim 10 - 250$ eV. Therefore, a large variation in the UV background spectrum among different models, especially at these energies, can have significant impact on the inferred properties of the CGM gas.

Most of the variation in the UV background models, as seen in Fig. 1, can be accounted by the difference in the emissivity of sources used as input. UV background models assume two types of sources; galaxies and quasars. At low redshifts $z \lesssim 2$, there is now consensus that the UV background (at $E > 13.6$ eV) is contributed by quasars alone ([Khaire & Srianand 2015](#); [Gaikwad et al. 2017a](#); [Kulkarni et al. 2018](#); [Khaire et al. 2019](#)), and hence the contribution from galaxies is negligibly small. Therefore, the variation in the UV

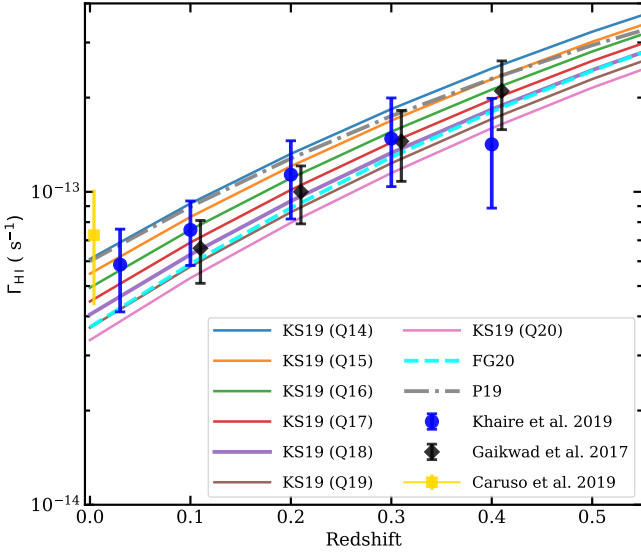


Figure 2. The H I photoionization rates (Γ_{HI}) with redshift ($z < 0.5$) for different UV background models along with the measurements (Gaikwad et al. 2017a; Khaire et al. 2019; Caruso et al. 2019). Solid lines show KS19 UV background models obtained by varying intrinsic quasar SED (a power-law $L_\nu \propto \nu^{-\alpha}$) index α from 1.4 (model Q14) to 2.0 (model Q20). All these models, including two new UV background models by P19 and FG20, are consistent with the Γ_{HI} measurements. Moreover, they encompass the whole $1 - \sigma$ range in the Γ_{HI} measurements.

background models seen at low- z (see Fig. 1) is primarily due to differences in the quasar emissivity. There are other factors such as the H I column density distribution used in the UV background models and also the model prediction of He II column densities (see Khaire & Srianand 2013), however their contribution to the variation in the UV background spectrum is subdominant as compared to the quasar emissivity at $z < 2$.

The main reason for differences in the quasar emissivity at $10 - 10^3$ eV is the lack of good constraints on the mean quasar SED. Quasar emissivity is modelled by using a power-law $L_\nu \propto \nu^{-\alpha}$ at $E \gtrsim 10$ eV whose reported measurements do not agree with each other and scatter in their values imprints large differences on the emissivity and hence on the UV background models. Even the most recent studies with large data-sets (Shull et al. 2012a; Stevans et al. 2014; Tilton et al. 2016; Lusso et al. 2015, 2018) report values of power-law index α ranging from 0.7 to 2.2 for mean quasar SED. Moreover, the highest energy at which the power-law SEDs are measured is less than 30 eV. Therefore, in absence of any constraints on the quasar SED for $E > 30$ eV, UV background models use the same power-law at $E > 13.6$ eV and extrapolate it till soft X-rays around 1 – 2 keV (KS19; P19). One exception is the new model by FG20, where author connected the SED at $E = 21$ eV to 1 keV which resulted into softer emissivity and therefore softer UV background at higher energies as compared to other models (see Fig. 1). Given the huge range in reported values of power-law index α for quasar SED, KS19 provided seven UV background models by varying α from 1.4 (model Q14) to 2.0 (model Q20) with an increment of 0.1. This small conservative range of $\alpha = 1.4 - 2$ as compared to the reported observations by different studies (i.e $\alpha = 0.7 - 2.2$) was chosen to be consistent with high- z observations of He II ($\alpha = 1.6 - 2.0$ from Khaire 2017) and to incorporate new low- z measurements of α by Shull et al. (2012a) and Stevans et al. (2014). All of these seven

models published in (KS19) at $z = 0.2$ are shown in Fig. 1. Every other parameters in these models are same and only the soft X-ray SED (at $E \gtrsim 1$ keV) has been modified for each model to match the X-ray background measurements (for more details see KS19). Whereas, both P19 and FG20 chose $\alpha = 1.7$ but latter used it till $E \sim 21$ eV only. Even though the quasar SED is same in three models Q17 of KS19, P19 and FG20, the UV background spectra are different because of differences in the input parameters such as quasar emissivity at 13.6 eV, its redshift evolution and the H I distribution in the IGM. As compared to the models of P19 and FG20, one of the advantage of using seven models of KS19 is that they differ only in terms of quasar SED (at $13\text{eV} \lesssim E \lesssim 1\text{keV}$ determined by α). Note that we are not synthesizing any new UV background models in this paper, rather we are just using existing models. For more details on individual models we direct readers to respective literature (i.e KS19; FG20; P19).

All the nine UV background models are physically viable options. This is illustrated in Fig. 2 where we show the predicted H I photoionization rates (Γ_{HI}) from all nine UV background models along with Γ_{HI} measurements at $z < 0.5$. Measurement of Γ_{HI} are shown from Khaire et al. (2019) and Gaikwad et al. (2017a) that are obtained using low- z Lyman- α forest (from Danforth et al. 2016) while Caruso et al. (2019) measurement used H- α fluorescence from outskirts of nearby galaxy UGC 7321. Despite different shapes, all nine UV background models are consistent with Γ_{HI} measurements. Moreover, these models approximately cover the range in Γ_{HI} measurements and their uncertainty. Therefore, these models are ideal set of models to find the systematic variation in the inferred CGM properties. Ideally, for CGM observations one should find the systematic uncertainty in the inferred quantities by using all these models, and quote it along with statistical uncertainty of the inferred quantities but it is not always feasible for individual CGM studies to do that. Therefore, in this paper we quantify the average systematic uncertainty on the inferred density and metallicity arising from UV background variation. For that we used toy CGM observations and two inference techniques as explained in the next section. Also note that there are still many studies that choose old UV background models such as Haardt & Madau (2012) and Faucher-Giguère et al. (2009) that are shown to be inconsistent with new observations (see Kollmeier et al. 2014; Shull et al. 2015; Khaire & Srianand 2015; Gaikwad et al. 2017a,b), which can add more to the systematic uncertainty in the inferred properties of the CGM.

3 TOY CGM OBSERVATIONS AND METHODS TO INFER THE DENSITY AND METALLICITY

In this section, we discuss our toy models that serve as mock CGM observations for photoionized and warm-hot gas. We also discuss two different methods to infer the hydrogen number density n_{H} (cm^{-3}) and metallicity Z/Z_\odot from those mock observations.

3.1 Toy models of photoionized and warm-hot absorbers

CLOUDY ionization models are routinely used for inferring hydrogen number density n_{H} (cm^{-3}) and metallicity Z/Z_\odot of CGM absorbers. In such models, these absorbers are assumed to represent plane parallel slabs of gas with uniform density and metallicity in a thermal and photoionization equilibrium with the extragalactic UV background. The basic methodology is to vary the density and metallicity in CLOUDY models to obtain a good agreement between model column

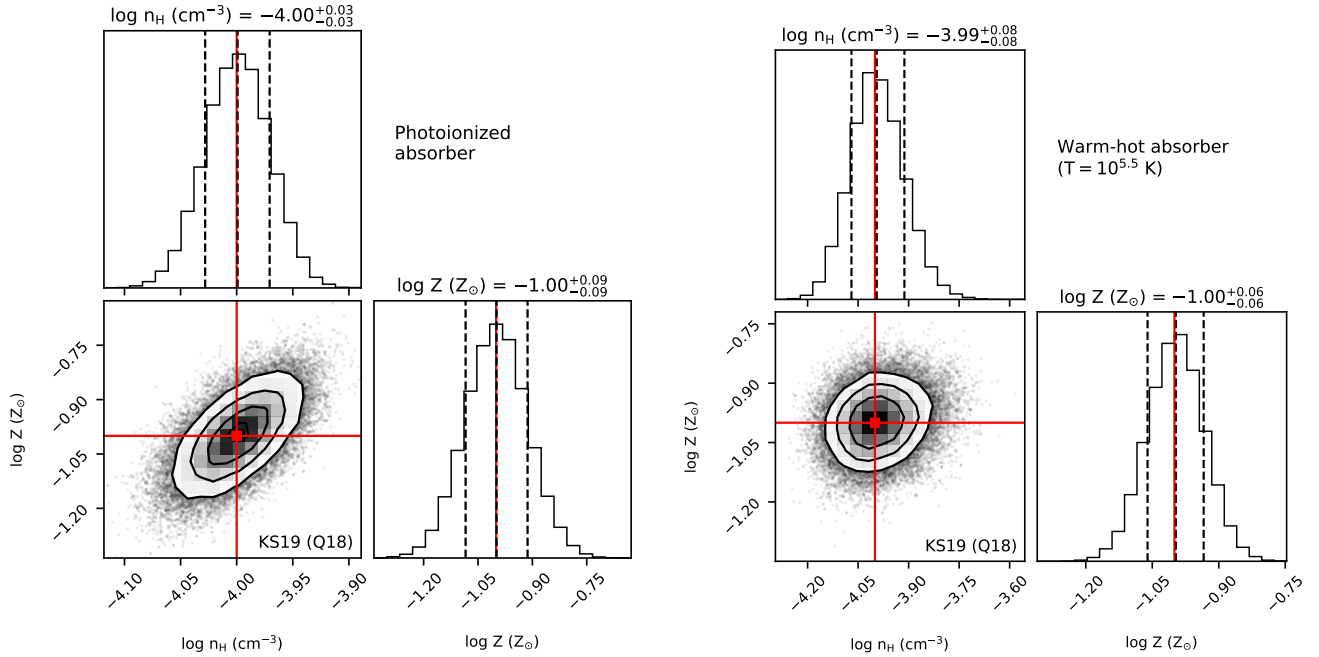


Figure 3. A joint posterior PDF of $\log n_{\text{H}} (\text{cm}^{-3})$ and $\log Z (Z_{\odot})$ along with their marginalized PDF are shown for the inference test for photoionized absorber (left-hand panel) and warm-hot absorber at $T = 10^{5.5} \text{ K}$ (right-hand panel). We use the same Q18 **KS19** UV background to infer the n_{H} and Z that is used in our toy model to create mock CGM observations. Red lines shows true values of $\log n_{\text{H}} (\text{cm}^{-3}) = -4$ and $\log Z (Z_{\odot}) = -1$ which are in excellent agreement with the median of marginalized PDFs as shown in the legends (with errors indicating a range of 16 and 84 percentiles).

densities and observed column densities of all ion-species in an absorber. Taking cue from this, we set up a plane parallel slab absorber in `CLOUDY v17.02` which is in ionization and thermal equilibrium with Q18 model of **KS19** (their fiducial model with $\alpha = 1.8$)

having hydrogen number density $n_{\text{H}} = 10^{-4} \text{ cm}^{-3}$ and metallicity $Z = 0.1Z_{\odot}$. This absorber is assumed to have neutral hydrogen column density $N_{\text{HI}} = 10^{15} \text{ cm}^{-2}$, which is used as a stopping criteria for the `CLOUDY` model. From the output of this `CLOUDY` model we note-down column densities of various metal ions. A set of column densities $\{\log N_{\text{ion}}^{\text{obs}}\}$ from those along with $N_{\text{HI}} = 10^{15} \text{ cm}^{-2}$ constitute our toy CGM observation. We call it as our ‘photoionized’ mock absorber. Later, we change these input values used for modelling mock absorber to provide general results.

Given the fact that a significant amount of gas in the IGM and CGM resides in a warm-hot $10^5 - 10^7 \text{ K}$ phase (see **Shull et al. 2012b**), we also generate another mock observations for such a gas. For that, we keep the plane parallel slab of gas at a constant temperature $T = 10^{5.5} \text{ K}$ and irradiated it with same Q18 **KS19** UV background in `CLOUDY`. All the other parameters in these `CLOUDY` models are same as the ‘photoionized’ mock absorber described above (i.e $n_{\text{H}} = 10^{-4} \text{ cm}^{-3}$, $Z = 0.1Z_{\odot}$ and $N_{\text{HI}} = 10^{15} \text{ cm}^{-2}$). Similar to the photoionized case, we note down the column densities of various metal ions from `CLOUDY` output, and use a small $\{\log N_{\text{ion}}^{\text{obs}}\}$ subset out of it along with $N_{\text{HI}} = 10^{15} \text{ cm}^{-2}$ as our mock observation for the warm-hot gas. We call it as a ‘warm-hot’ mock absorber. In all `CLOUDY` models (ran for mock observations as well as for the inference), we take solar abundance of heavy elements from **Grevesse et al. (2010)**. We also scale the elemental helium abundance by a factor 8.163×10^{-2} so that the ratio of hydrogen to helium number density ($n_{\text{H}}/n_{\text{He}}$) becomes 12.25, consistent with recent measurements of helium mass fraction $Y_p = 0.246^{+0.039}_{-0.041}$ (where $n_{\text{H}}/n_{\text{He}} = 4(1 - Y_p)/Y_p$) from cosmic microwave background (**Planck**

Collaboration et al. 2018, with TT+ LowE). Without such a scaling the default elemental abundance of helium in `CLOUDY` represents the one typically found in the interstellar medium i.e $n_{\text{H}}/n_{\text{He}} = 10$.

3.2 Methods to jointly constrain n_{H} and Z

First, we ran a huge grid of `CLOUDY` simulations with an equally spaced dense grid of $\log n_{\text{H}}$ (from -5 to -2 with $\Delta \log n_{\text{H}} = 0.02$) and $\log Z$ (from -3 to 1 with $\Delta \log Z = 0.05$). We repeat such a simulation grid for all nine UV background models. For each UV background used in the `CLOUDY` model, we stored the model predicted column densities of metal ions $\{\log N_{\text{ion}}^{\text{uvb}}\}$ for every input parameter $\theta^{\text{uvb}} \equiv (\log n_{\text{H}}, \log Z)$. Then, using methods described below we compare $\{\log N_{\text{ion}}^{\text{uvb}}\}$ to the $\{\log N_{\text{ion}}^{\text{obs}}\}$ in order to infer the parameters θ^{uvb} .

We developed two methods that use our toy observations (a set of ion column densities $\{\log N_{\text{ion}}^{\text{obs}}\}$) and our `CLOUDY` model grid to infer the n_{H} and Z for different assumed UV background models. First method uses Bayesian formalism along with MCMC to explore the posterior probability density function (PDF) of parameters n_{H} and Z . This method was used to mimic the real observations where observed column densities have uncertainties. To mimic that, we use errors drawn from a Gaussian distribution on the mock observed column densities. In the second method, we determine n_{H} and Z by simply minimizing the least square difference between the observed and modelled column densities of metal ions. We later show that, results of both methods are in excellent agreement. These methods are described below.

In our first method, using Bayes theorem we write down the

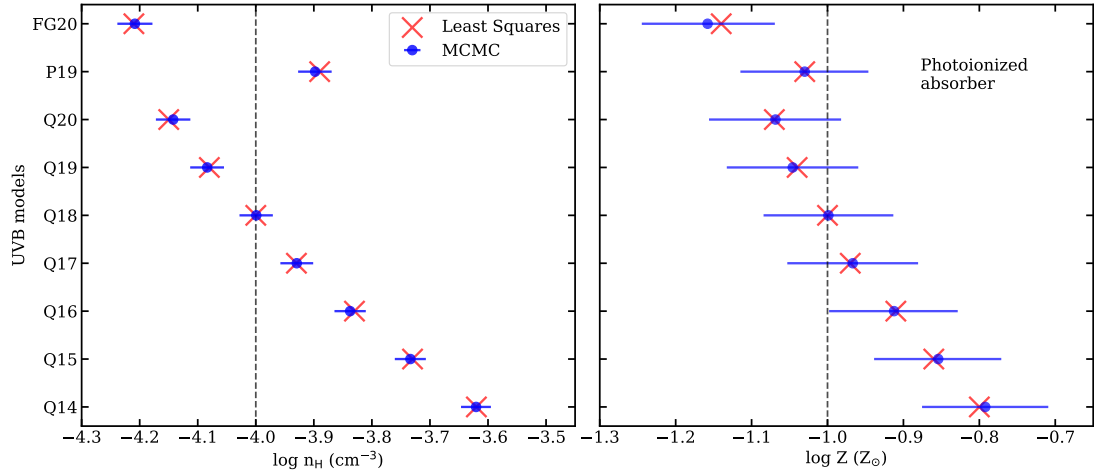


Figure 4. Inferred values of n_{H} (cm^{-3} ; left-hand panel) and Z/Z_{\odot} ; right-hand panel) with different UV background models (labeled on y-axis; see Fig. 1) for the test-case of a photoionized absorber. We use column densities of five ions $\{N_{\text{CIV}}, N_{\text{NV}}, N_{\text{OVI}}, N_{\text{SiIV}}, N_{\text{NeVIII}}\}$ for the inference. Models Q14-Q20 are from KS19. The circles with horizontal error-bars show the result from the Bayesian MCMC method (median with 16 and 84 percentile values of posterior PDF; see Fig. A1 for few illustrations) while the red crosses shows the result of least square minimization method. Vertical dashed lines indicate the true values from toy observations which used Q18 KS19 UV background model. The total difference in the inferred density $\Delta_{\text{max}}(\log n_{\text{H}}) = 0.66$ and metallicity $\Delta_{\text{max}}(\log Z) = 0.48$ across all UV background models.

posterior PDF as

$$P(\{\log N_{\text{ion}}^{\text{uvb}}\}(\theta^{\text{uvb}})|\{\log N_{\text{ion}}^{\text{obs}}\}) \propto P(\{\log N_{\text{ion}}^{\text{obs}}\}|\{\log N_{\text{ion}}^{\text{uvb}}\}(\theta^{\text{uvb}}))P(\{\log N_{\text{ion}}^{\text{uvb}}\}(\theta^{\text{uvb}})), \quad (1)$$

where we chose priors $P(\{\log N_{\text{ion}}^{\text{uvb}}\}(\theta^{\text{uvb}}))$ to be flat for both parameters $\log n_{\text{H}}$ and $\log Z$. We use likelihood $\mathcal{L} \equiv P(\{\log N_{\text{ion}}^{\text{obs}}\}|\{\log N_{\text{ion}}^{\text{uvb}}\}(\theta^{\text{uvb}}))$ to be Gaussian as

$$\mathcal{L} = \prod_i \frac{1}{\sqrt{2\pi}\sigma_i} \exp\left(-\frac{(\log N_i^{\text{uvb}}(\theta^{\text{uvb}}) - \log N_i^{\text{obs}})^2}{2\sigma_i^2}\right). \quad (2)$$

Here, index i represents a metal ion from the set of ions chosen for the inference (i.e the set of ions in mock observations) and σ_i is the error on $\log N_i^{\text{obs}}$. For our toy observations we generate random Gaussian errors σ_i within a range 0.01 – 0.25 dex.¹ We then use MCMC (the emcee code by Foreman-Mackey et al. 2013) to sample the posterior PDF by interpolating between our dense CLOUDY model grids.

First we perform the inference test where we use the same Q18 KS19 UV background in CLOUDY models to check how close our inferred values get to the true values. The results of such inference test are shown in the Fig. 3 for both photoionized absorber as well as $10^{5.5} \text{K}$ warm-hot absorber. For both inferences, we use the same set of five metal ion column densities in observations; $\{N_{\text{CIV}}, N_{\text{NV}}, N_{\text{OVI}}, N_{\text{SiIV}}, N_{\text{NeVIII}}\}$. Fig. 3 shows that the median of marginalized $\log n_{\text{H}}$ and $\log Z$ values are in excellent agreement with true values -4 and -1 , respectively.

We reproduce the same results with a random choice of any two or more metal ions from a large set of metal ions. We find that to jointly constrain the n_{H} and Z we need to use at least two metal ions and they need not to be from the same element.

¹ We note that the inferred median of posterior does not depend on the values of the errors but the confidence interval scales with them. Also, we just assign Gaussian errors to the column densities without altering their values.

We find that when we use same UV background model as in the mock observations the inferred median values of n_{H} and Z always match with the true values (within 0.01 dex) for both photoionized absorber and warm-hot absorber with $T \lesssim 10^{6.5} \text{K}$. For high temperature gas $T \gtrsim 10^{5.75} \text{K}$, however, we need to reduce the error on our mock column densities to unrealistically small values to pass an inference test. Therefore, we restrict our-self to the warm-hot absorber models with $T = 10^{5.5} \text{K}$. However it is interesting to see how the joint posteriors of n_{H} and Z changes with the T , which is explored in Fig. A2 of the appendix.

Although the Bayesian MCMC approach is best suited for real observations which has Voigt profile fitting errors on column densities, the median values of parameters (n_{H} and Z) can be simply obtained by minimizing the least square difference, denoted by LS here,

$$LS(\theta^{\text{uvb}}) = \sum_i (\log N_i^{\text{uvb}}(\theta^{\text{uvb}}) - \log N_i^{\text{obs}})^2, \quad (3)$$

between the observed and model column densities. The least square fitting approach is also computationally least expensive. We confirm that we reproduce the true values of n_{H} and Z using this method. Later, for quantifying the uncertainty on the inferred values of n_{H} and Z from different assumed UV background models we use both methods, results of which are discussed in the next section.

4 RESULTS AND DISCUSSIONS

In this section, we present the result of our analysis for both photoionized and warm-hot CGM gas. We first show the results for a test case where we use the same set of ions used for inference test (as shown in Fig. 3) and then discuss results where we use different sets of ions to quantify the distribution of inferred n_{H} and Z . We also discuss the effect of shape and normalization of UV background spectra on the inferred n_{H} and Z .

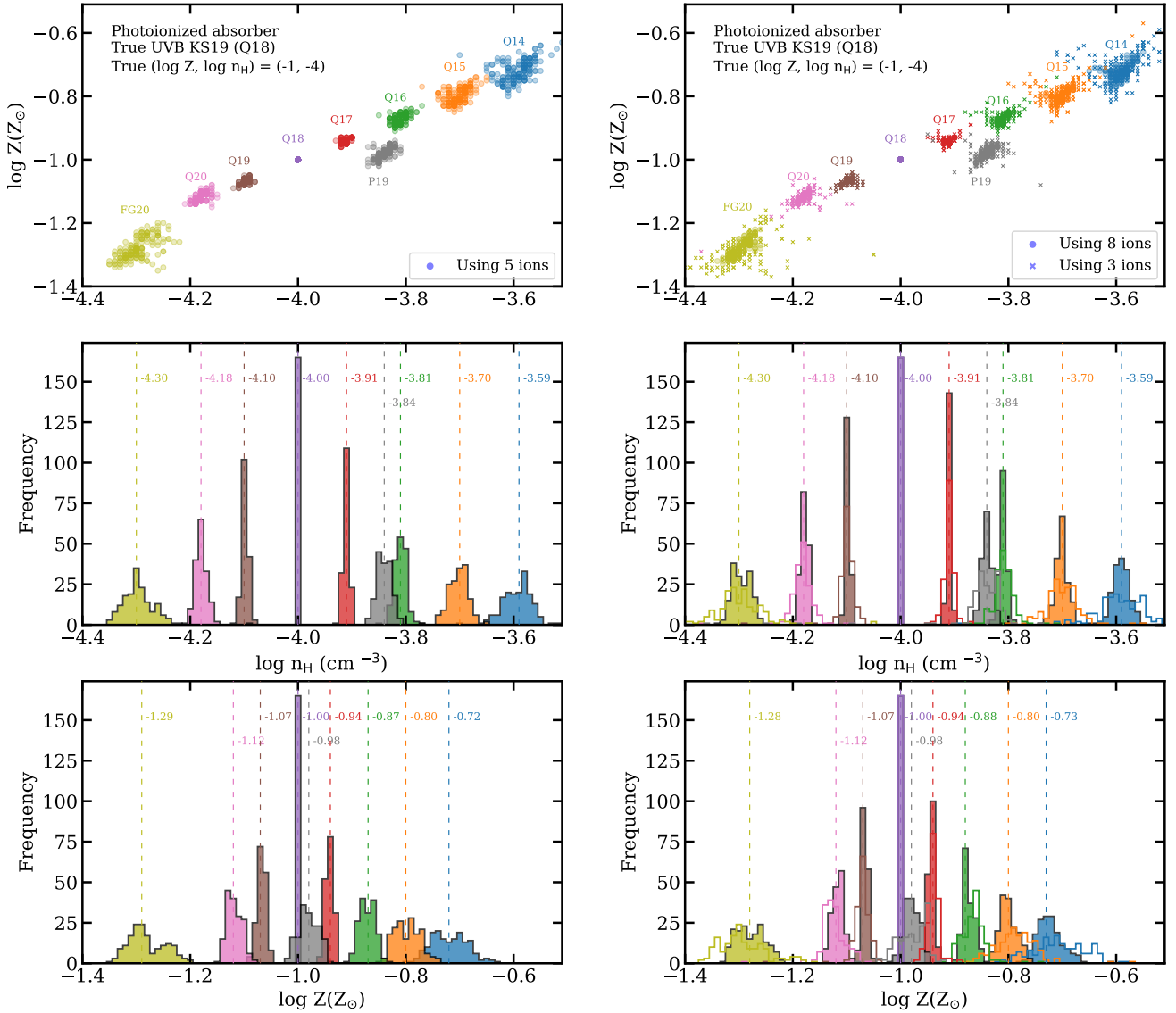


Figure 5. Distribution of inferred n_{H} and Z for photoionized mock absorber obtained using 165 sets of five ions (left-hand panel), three ions and eight ions (right-hand panels.) Top panels show joint n_{H} and Z values whereas middle and bottom panels show the histograms of n_{H} and Z , respectively. Different colors are used for different UV backgrounds. Vertical dashed lines and annotated values close to it show the median of the distributions. In both panels, true values of n_{H} and Z are 10^{-4} cm^{-3} and $Z = 10^{-1} Z_{\odot}$ and Q18 KS19 UV background. In the right-hand side top panel shows n_{H} and Z inferred from three ions with crosses and their distributions with open histograms at the middle and bottom panels, and from eight ions with circles and their distribution with solid histograms at the middle and bottom panels. From this, it is evident that higher the number of ions, the better are the individual constraints of n_{H} and Z . Note that the width of individual histogram is significantly smaller than the variation in n_{H} and Z arising from all UV background models. Here, $\Delta_{\text{max}}(\log n_{\text{H}}) = 0.71$ dex and $\Delta_{\text{max}}(\log Z) = 0.56$ dex (for all nine UV background models) when we use eight ions for the inference.

4.1 Photoionized Absorbers

For a test case, inferred values of the n_{H} and Z obtained using both Bayesian and least square methods by assuming different UV background models are shown in Fig. 4 for our photoionized mock absorber. For this particular example, we used the same set of five ions as we used in the inference test (Fig. 3). Median values of n_{H} and Z from MCMC Bayesian fits match very well with the values obtained from least square minimization. We note that the size of confidence intervals on n_{H} and Z , i.e. the 16 and 84 percentile values of the posterior PDFs, scales with the error on the metal-ion column densities, whereas the median values of inferred n_{H} and Z remain same. In Fig. A1 of the appendix, we show a few example

posterior PDFs for the Bayesian MCMC inference whose results (marginalized n_{H} and Z values with confidence intervals) are shown in Fig. 4. The expected variation in the inferred n_{H} and Z values can be seen in Fig. 4. For photoionized models the true n_{H} and Z (shown by vertical dashed lines in Fig. 4) are reproduced only when the true UV background model, Q18 KS19, is used in the cloudy. The total variation in the inferred n_{H} is 0.57 dex across the seven UV background models of KS19 and 0.66 dex if we include remaining two UV background models. Whereas variation in Z is less as compared to variation in n_{H} , it is 0.35 dex for seven KS19 models and 0.48 dex across all nine UV background models. The inferred values of n_{H} and Z for P19 lie close to the inferred values for Q16-Q18 models of KS19. A possible reason for this is

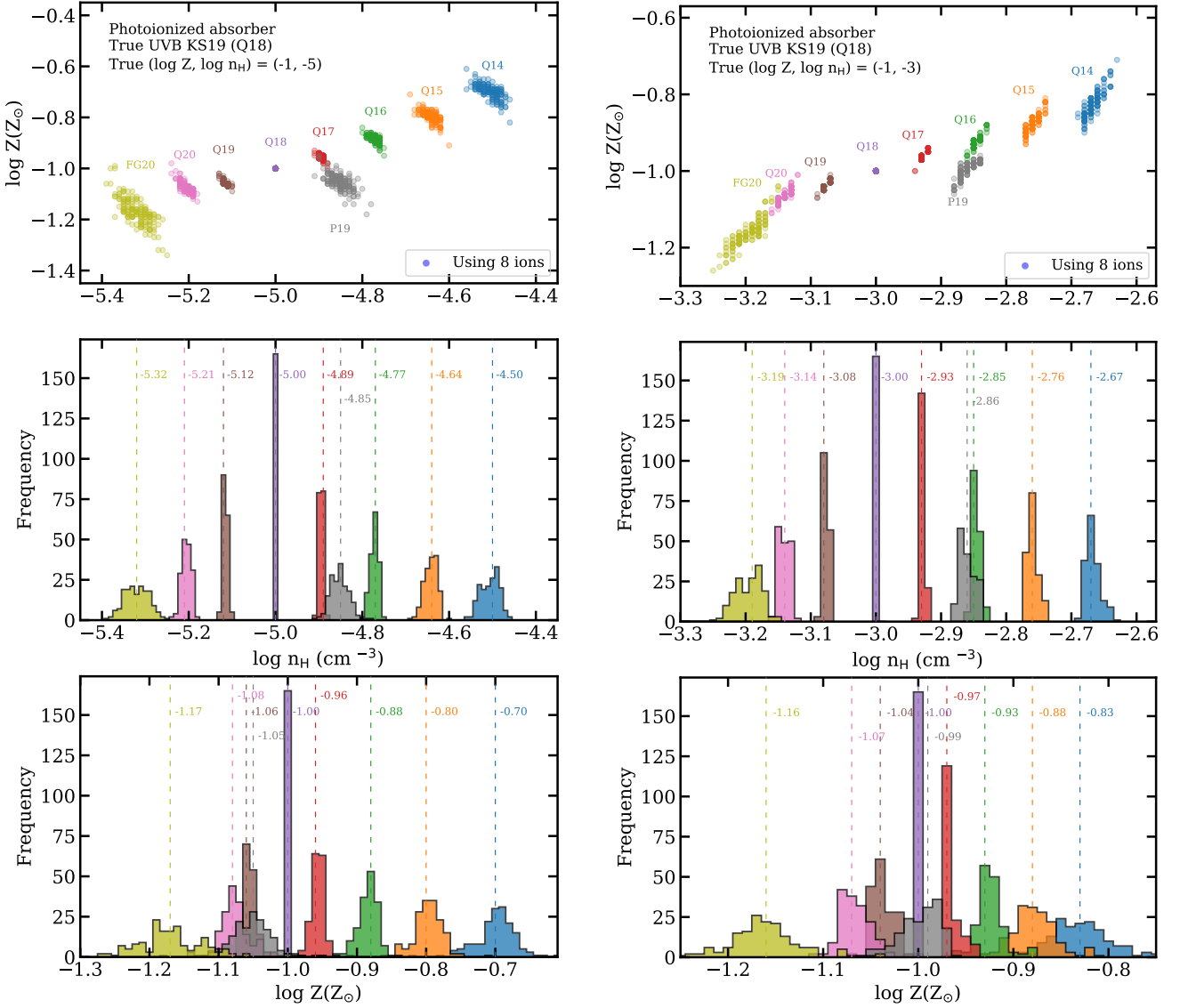


Figure 6. Same as Fig. 5 but for true value of $Z = 10^{-1}Z_{\odot}$ and $n_{\text{H}} = 10^{-5} \text{ cm}^{-3}$ (left-hand panel) and 10^{-3} cm^{-3} (right-hand panel) obtained with 165 sets of eight ions. Here, total variation $\Delta_{\text{max}}(\log n_{\text{H}}) = 0.82$ and $\Delta_{\text{max}}(\log Z) = 0.47$ in left-hand panel and $\Delta_{\text{max}}(\log n_{\text{H}}) = 0.52$ and $\Delta_{\text{max}}(\log Z) = 0.33$ in right-hand panel which indicates that with increasing density (i.e. higher true n_{H}) the variation in the inferred n_{H} and Z arising from uncertain UV background decreases.

discussed in section 4.3. The softest UV background FG20 provides lowest values of n_{H} and Z . Fig. 4 shows a clear trend that the softer UV background models (refer to Fig. 1) leads to the lower values of inferred n_{H} and Z . It is especially apparent in seven model of KS19 where the shape of UV background depends only one one parameter i.e the intrinsic SED (α) of QSOs. Such a trend can be naively explained in terms of the ionization parameter U . Because for optically thin cloud the abundance pattern of ions depends on the ionization parameter $U = n_{\gamma}/n_{\text{H}}$ of hydrogen, where number density of hydrogen ionizing photons n_{γ} reduces with increasing α . Therefore, for softer UV background with higher α the inferred n_{H} decreases to preserve U in order to reproduce ion column densities as in mock observations.

To understand the dependence of our inferred n_{H} and Z on the choice of different ions used in the mock observations, we use a large number of different sets of ions and infer n_{H} and Z . For that, we first identify ions whose column densities are more than 10^{11} cm^{-2}

in a cloudy model ran with $n_{\text{H}} = 10^{-4} \text{ cm}^{-3}$ and $Z = 0.1 Z_{\odot}$ with true UVB as (KS19) Q18 out of 23 different metal ions commonly observed in the CGM across all redshifts.² We select minimum column density threshold 10^{11} cm^{-2} to avoid very low columns of ions produced in cloudy models and verified that our final results are not sensitive to this threshold as long as it is larger than 10^{11} cm^{-2} . Then, out of these selected ions we create all possible sets of different ions with varying number of ions in each set. We then group these sets according to number of ions they have, from two ions to eight ions. From such sets with a fixed number of ions we randomly pick 165 unique sets.³ Next, we use column densities of

² The 23 ions considered are: C II, C III, C IV, N III, N IV, N V, O II, O III, O IV, O V, O VI, O VII, S II, S III, S IV, S V, S VI, Si II, Si III, Si IV, Mg II, Ne VIII and Fe II.

³ The number 165 is arrived at by firstly choosing the minimum number of ions that satisfy the above screening criteria, with the stopping criteria set

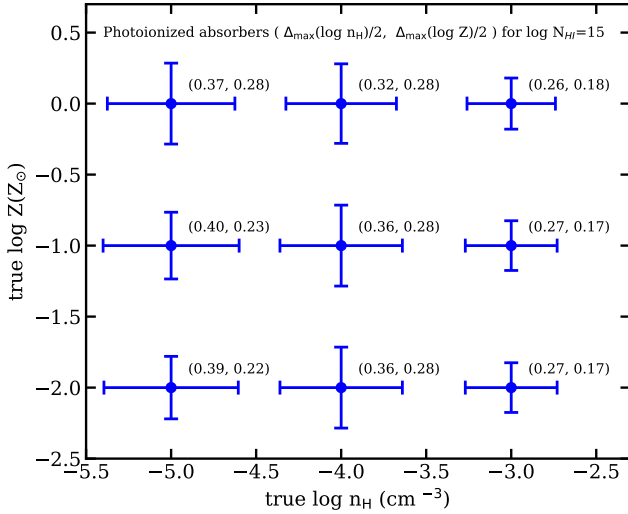


Figure 7. The grid of true n_{H} and Z where the extent of error-bars show the uncertainty (Δ_{max} values) on the inferred n_{H} (horizontal error-bars) and Z (vertical error-bars) arising from uncertain UV background (using all nine UV background models) for photoionized gas. The annotated values in the brackets show the $\Delta_{\text{max}}(\log n_{\text{H}})/2$ and $\Delta_{\text{max}}(\log Z)/2$ which can be quoted as systematic uncertainty on the inferred values of n_{H} and Z from CGM observations for absorber with $N_{\text{HI}} = 10^{15} \text{ cm}^{-2}$. These Δ_{max} values are also given in Table 1. See Fig. B1 for the results obtained for absorbers with N_{HI} ranging from 10^{14} to 10^{19} cm^{-2} .

these ions (from our toy CGM absorber) in each set and treat it as one mock observation to infer the n_{H} and Z assuming all nine UV background models. For such inferences we use the least square minimization method since it is computationally efficient and the results agree very well with the Bayesian MCMC method.

The distributions of the inferred n_{H} and Z are shown in Fig. 5 for all nine UV background models where our mock CGM absorber had true values of $n_{\text{H}} = 10^{-4} \text{ cm}^{-3}$ and $\log Z = -1$ with Q18 (KS19) as a true UV background. Top panels of Fig. 5 show inferred values of n_{H} and Z for 165 sets of five (left-hand panel), three and eight (right-hand panel) metal ions each. Middle and bottom panels show the distributions of inferred n_{H} and Z for each UV background model. First thing to note that no matter how many ions and which set of ions we use, we always get back the true n_{H} and Z when we use true UV background model in CLOUDY, as evident from δ -function like histograms for Q18 models. When we use different UV background model, we see that different set of ions give slightly different results. The scatter in these results widens the distribution of inferred n_{H} and Z , especially apparent when we use the UV background that is quite different than the true UV background. It is rather interesting to note that distributions of n_{H} and Z widens monotonically as we move to softer or harder UV background models, except for P19. This interesting trend is apparent in the results obtained for all sets of ions with different numbers, be it three ions or eight ions (see right-hand panel of Fig. 5). Such a trend can be used to constrain the true model of UV background by using CGM observations which we plan to explore in our future work.

Fig. 5 also shows the expected trend that when we use more ions, e.g eight as compared to three as shown in right-hand panel of

the figure, the constraints on n_{H} and Z become better. In other words, the scatter around the median inferred value of n_{H} and Z reduces when one uses sets of ions with a larger number of ions for the inference. This can be seen from right-hand panels of Fig 5 where filled histograms obtained for 165 sets of eight ions are narrower than the the open histograms obtained for 165 sets of three ions. However, note that this scatter around the median value (i.e the width of distribution) for both inferred n_{H} and Z is significantly lower as compared to the differences in the median values for the range of UV background models, even when we use sets of just three ions. Therefore the uncertain UV background can have major contribution in the total uncertainty of the inferred n_{H} and Z . Dotted lines in the middle and bottom panels indicate the median values of the inferred n_{H} and Z which are also annotated on the figure with same colors. We note that the median values converge within 0.01 dex when we use more than four ions to infer mean n_{H} and Z , but even if we use only three or four ions the median values differ by less than 0.05 dex from the converged values. We do not recommend using only two ions, unless they are from the same element, because in that case the scatter in the inferred values of n_{H} and Z can be of the order of a magnitude.

In Fig. 5, we see the same trends in the median values of inferred n_{H} and Z as in the test case shown in Fig 4, i.e the softer UV background yields lower n_{H} and Z . To quantify the total variation in the inferred n_{H} and Z values across different UV background models we define $\Delta_{\text{max}}(\log n_{\text{H}})$ and $\Delta_{\text{max}}(\log Z)$. These quantities represent the expected variation in the n_{H} and Z due to uncertain UV background. The values of $\Delta_{\text{max}}(\log n_{\text{H}})$ and $\Delta_{\text{max}}(\log Z)$ are obtained by taking the difference in the median of inferred n_{H} and Z values for each UV background model and then finding out the maximum of that difference. Given the trend of inferring lower values of n_{H} and Z with softer UV background, the Δ_{max} values when quoted for all nine UV background models, are just the differences between median inferred n_{H} and Z obtained for Q14 KS19 and FG20 models. Whereas, when we quote the Δ_{max} values for only seven KS19 UV background models, they represent the difference between inferred n_{H} and Z obtained for Q14 and Q20 models of KS19.

From Fig. 5, we find that $\Delta_{\text{max}}(\log n_{\text{H}}) = 0.59$ dex and $\Delta_{\text{max}}(\log Z) = 0.39$ dex for the seven UV background models of KS19. For all nine UV background models, we find $\Delta_{\text{max}}(\log n_{\text{H}}) = 0.71$ dex and $\Delta_{\text{max}}(\log Z) = 0.56$ dex. These results are obtained by using sets of eight ions for the inference (see right-hand panel of Fig. 5), the true values of n_{H} and Z as 10^{-4} cm^{-3} and $0.1Z_{\odot}$, and for true Q18 KS19 UV background. In order to check the dependence of different values of true n_{H} and Z used for creating the mock CGM absorber on the values of Δ_{max} , we redo the analysis for nine combinations of true n_{H} and Z where we change n_{H} from 10^{-5} to 10^{-3} cm^{-3} and Z from 0.01 to $1 Z_{\odot}$. Results for two such combinations ($\log Z = -1$ and $\log n_{\text{H}} = -3$, $\log Z = -1$ and $\log n_{\text{H}} = -5$) are shown in Fig. 6 where the n_{H} and Z inference used 165 sets of eight ions. The Δ_{max} values differ for these two cases by a factor of ~ 0.2 dex.

We find that for the same true n_{H} and Z there is a small change in Δ_{max} values of the order of 0.1 dex if we use different true UV background models, instead of fiducial Q18 KS19 model, in our mock CGM absorbers (as described in sec. 3.1). Therefore, we repeat the analysis by changing the true UV background models and calculate Δ_{max} values. We do this for all nine UV background models and take the mean of the Δ_{max} values.⁴ These mean values of

to $N_{\text{HI}} = 10^{14.5} \text{ cm}^{-2}$ which is found to be 11. Then, the number of largest possible sets of 8 ions each is ${}^{11}\text{C}_8 = 165$.

⁴ Note that we take mean for just removing the dependence on a true UV

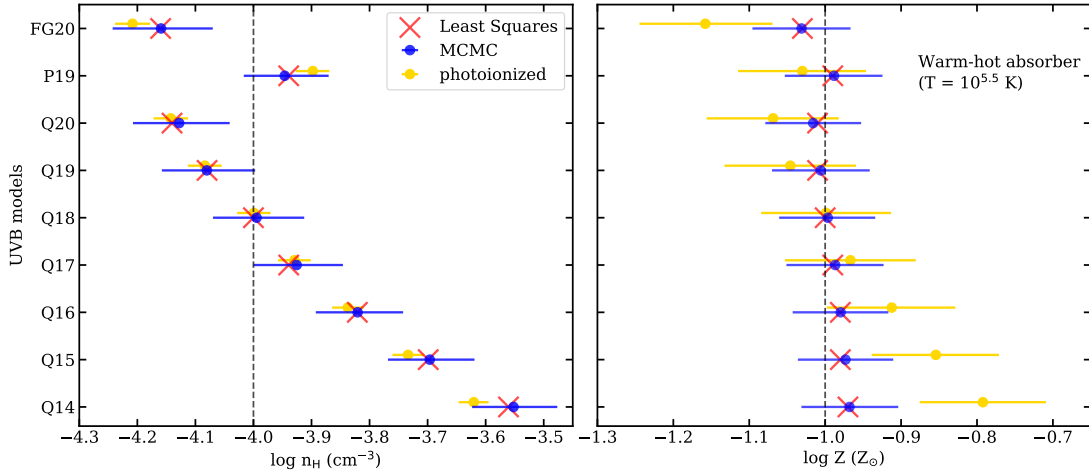


Figure 8. Inferred values of n_{H} (cm^{-3} ; left-hand panel) and Z (Z_{\odot} ; right-hand panel) with different UV background models (labeled on y-axis; see Fig. 1) for the warm-hot absorber with $T = 10^{5.5}$ K. Models Q14-Q20 are from KS19. The circles with horizontal error-bars show the result from the Bayesian MCMC method (median with 16 and 84 percentile values of posterior PDF) while the red crosses shows the results from least square minimization method. Vertical dashed lines indicate the true values from toy observations generated using Q18 KS19 UV background model. The total difference in the inferred density $\Delta_{\text{max}}(\log n_{\text{H}}) = 0.55$ while the metallicity does not show any significant deviation ($\Delta_{\text{max}}(\log Z) = 0.03$) from the true value. Yellow color data points show the result for photoionized absorber test case (from Fig. 4) for comparison.

$\Delta_{\text{max}}(\log n_{\text{H}})$ and $\Delta_{\text{max}}(\log Z)$ are given in Table 1 and also shown in Fig. 7 with error-bars on the true values of n_{H} and Z . The full extent of error-bars in the figure represent the values of Δ_{max} . The annotated values in the figure are the $\Delta_{\text{max}}(\log n_{\text{H}})/2$ and $\Delta_{\text{max}}(\log Z)/2$ which is equivalent to being a systematic uncertainty on the $\log n_{\text{H}}$ and $\log Z$ arising from uncertain UV background. Fig. 7 shows that $\Delta_{\text{max}}(\log n_{\text{H}})$ and $\Delta_{\text{max}}(\log Z)$ has very weak dependence on true value of Z but both reduce by ~ 0.2 dex when true n_{H} changes from 10^{-5} to 10^{-3} cm^{-3} . The n_{H} and Z are better constrained for gas at high densities than at low densities. This is mainly because at high densities self-shielding of gas reduces the impact of UV background.

Till now we have assumed that the absorber is optically thin with hydrogen column density $N_{\text{HI}} = 10^{15}$ cm^{-2} which is not true for most of the CGM absorbers. Therefore we repeat the whole analysis with another sets of CLOUDY models by varying N_{HI} from 10^{14} to 10^{19} cm^{-2} . The results of which, similar to the one shown in the Fig. 7 are summarized in the Fig. B1 in Appendix.

Overall, for the absorbers in photoionization equilibrium, the inferred n_{H} can be uncertain up to a value of $\Delta_{\text{max}}(\log n_{\text{H}})$ which ranges from 0.5 to 0.8 dex and inferred Z can be uncertain up to a value of $\Delta_{\text{max}}(\log Z)$ that ranges from 0.2 to 0.6 dex for the gas with density 10^{-3} to 10^{-5} cm^{-3} for clouds with N_{HI} ranging from 10^{14} to 10^{19} cm^{-2} (see Fig. B1). Table 1 provides values of Δ_{max} for different true n_{H} and Z for all nine UV background (shown in Fig 7) as well as for only seven KS19 UV background models for absorber with $N_{\text{HI}} = 10^{15}$ cm^{-2} .

4.2 Warm-hot Absorber

In Fig. 8, we show the inferred values of the n_{H} and Z using both Bayesian MCMC and least square methods for a test case of a warm-hot absorber at constant temperature of $10^{5.5}$ K. For the inference,

background, so that one can quote $\pm\Delta_{\text{max}}(\log n_{\text{H}})/2$ as an average systematic error from UV background irrespective of their choice of UV background used for inference (but see Section 4.4).

we used the same set of five ions used in the inference test (Fig. 3) and the test case of a photoionized absorber (Fig. 4). As in the photoionized case, median values of n_{H} and Z from MCMC Bayesian fits match well with the values obtained from least square minimization. For comparison, we also show the Bayesian MCMC results obtained for the photoionized absorber (as shown in Fig. 4) with yellow data points. We get almost same n_{H} values as in case of the photoionized absorber. It suggests that the extra ionization of gas contributed by UV background in addition to collisional ionization is responsible for the change in inferred n_{H} . The total variation in n_{H} is 0.56 dex, just 0.1 dex smaller than the one obtained for test case of photoionized absorber. However, constraints on n_{H} become much weaker, as revealed by the extent of confidence intervals on blue and yellow points. We see similar trend in Bayesian MCMC posteriors at higher temperatures where the constraints become weaker for n_{H} and one needs to reduce the uncertainty on column densities of metals to get meaningful constraints. In Fig. A2 of appendix, we show few example posteriors obtained for the inference test of warm-hot absorber up to $T = 10^{6.5}$ K.

Inferred Z values for this test case of warm-hot absorber are consistent with the true Z and show very little variation across all UV background (maximum of 0.03 dex). This suggests that the effect of collisions dominates over the effect of photoionization for metals. The constraints on Z are slightly better than the one obtained for photoionized absorber, as can be seen from the extent of confidence interval.

To understand the dependence of our inferred n_{H} and Z on the choice of different ions, we follow the same procedure as in case of photoionized absorber and create 165 sets of ions with a fix number of ions in each set. We use these sets for the inference where the column densities of ions in each set obtained from our toy CGM warm-absorber serve as an individual mock observation. We use least square minimization for the inference. Results of which, obtained with sets of eight ions each, are shown in the left-hand panel of Fig. 9. For clarity we only show results obtained for Q14, Q16, Q18 of KS19 and FG20 UV background models. Here, we have true $n_{\text{H}} = 10^{-4}$ cm^{-3} and $Z = 10^{-1}Z_{\odot}$ with Q18 KS19 as a true UV

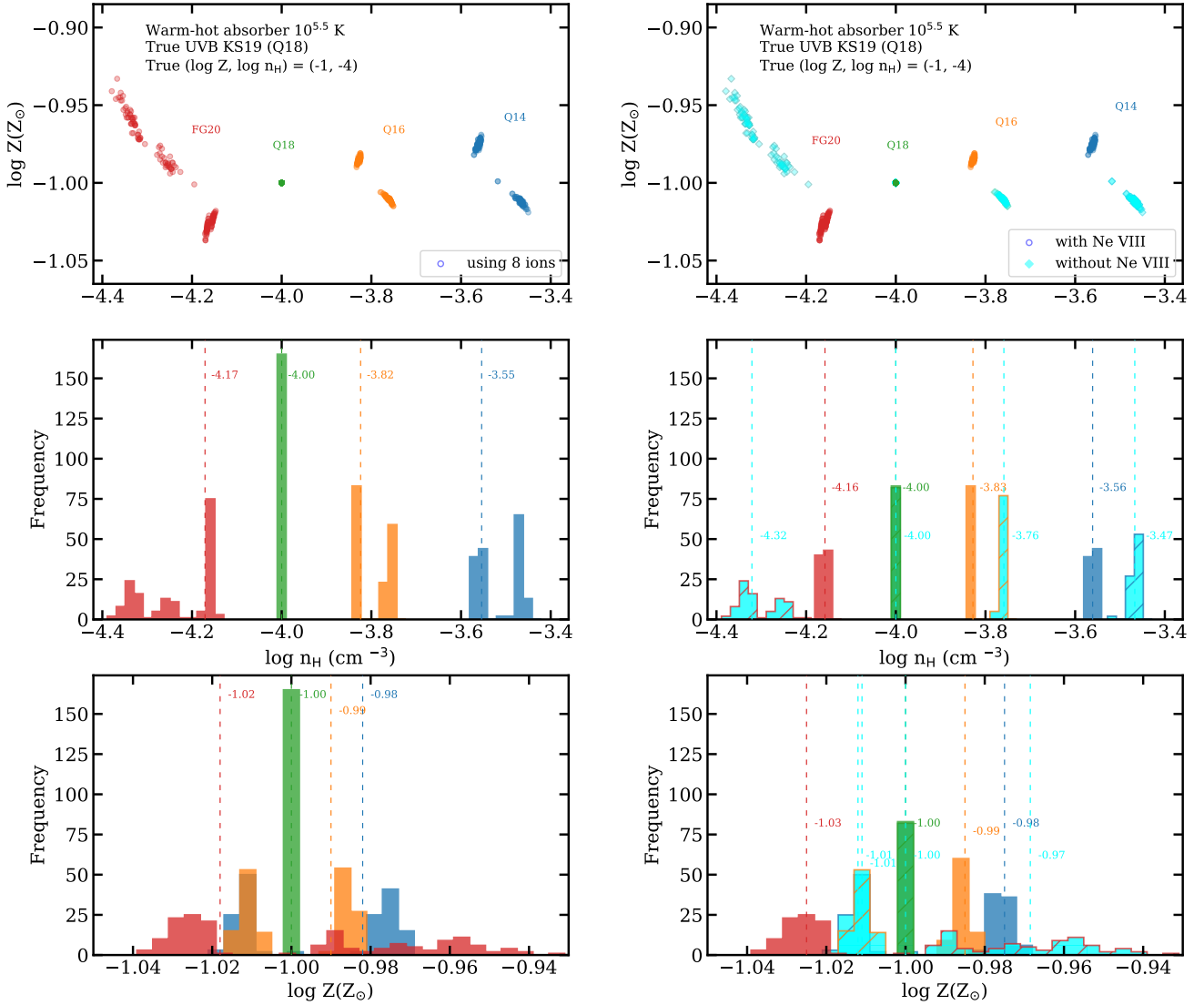


Figure 9. *Left-hand panels:* Distribution of inferred n_{H} and Z for warm-hot mock absorber at $T = 10^{5.5}$ K obtained using 165 sets of eight ions. Top panels show joint n_{H} and Z values whereas middle and bottom panels show the histograms of n_{H} and Z , respectively. Different colors are used for different UV backgrounds. Vertical dashed lines and annotated values close to those are the median values of the distributions. There is a clear bi-modality in the inferred n_{H} and Z values, except when we use the true UV background model. *Right-hand panel:* Same as left-hand panel but cyan points and histogram show the inferred n_{H} and Z obtained using set of ions not having Ne VIII (82 out of 165). All the cyan points fall on one side of bi-modal distribution indicating inclusion or exclusion of Ne VIII gives rise to the bi-modality. Moreover, inferred n_{H} is closer to true value when Ne VIII is included in the inference. Total variation in n_{H} is 0.6 dex when Ne VIII is included in the inference and 0.85 dex otherwise. Note that, irrespective Ne VIII, inferred Z is close to true Z within 0.03 dex.

background. Top panel shows individual n_{H} and Z values whereas middle and bottom panel shows the histograms of those. When we use same Q18 *KS19* UV background we reproduce true values all the time, as can be seen from the δ -function like histograms for n_{H} and Z . For other UV background models, not all sets of ions infer the same n_{H} and Z resulting into wider distributions. However, unlike photoionized absorber we find that the distributions of inferred n_{H} and Z are bi-modal for UV background models apart from the true Q18 UV background. This is more clear for the Q14 and Q16 UV background in the left-hand middle panel of Fig. 9. We found that this bi-modality is related to ion Ne VIII. If we split all 165 sets of ions in two groups, one group including Ne VIII (total of 83 sets) and other without it (82 sets), inferred values of n_{H} from these two groups clearly fall on two sides of the histogram explaining the

bi-modal nature of the original distribution. This is illustrated in right-hand panel of Fig. 9 where n_{H} and Z inferred excluding Ne VIII ion are shown with cyan color. Note that there is no bi-modality in inferred n_{H} and Z when we use the same true UV background model. Most interestingly, the set of ions having Ne VIII column densities always infer the n_{H} values close to true values as can be seen from the right-hand middle panel of the Fig. 9. Without Ne VIII, the true n_{H} can be off by factor of 0.1-0.16 dex. From Fig. 9, we find that $\Delta_{\text{max}}(\log n_{\text{H}}) = 0.85$ dex without including Ne VIII and 0.6 dex when including Ne VIII for all nine UV background models. Inferred metallicity, being very close to true values, does not show any significant dependence on the Ne VIII. In both cases, with and without Ne VIII, $\Delta_{\text{max}}(\log Z)$ is very small (< 0.05 dex). Note that

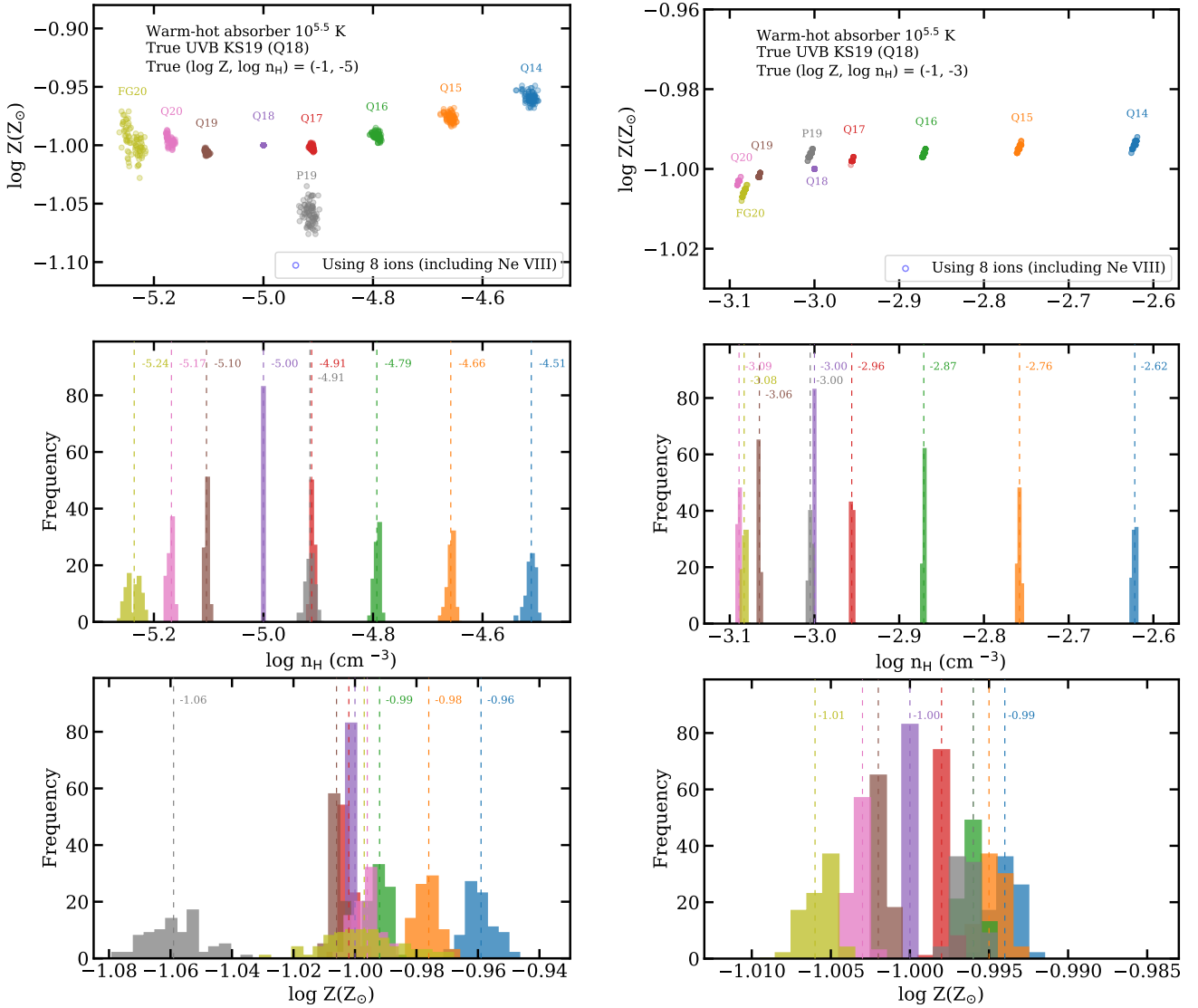


Figure 10. Same as the left-hand panel of Fig.9 but inferred n_{H} and Z shown only for 83 sets of ions out of 165 that have Ne VIII. Left-hand panel show results for true $n_{\text{H}} = 10^{-5} \text{ cm}^{-3}$ and right-hand panel shows results for true $n_{\text{H}} = 10^{-3} \text{ cm}^{-3}$. For both cases true $Z = 10^{-1} Z_{\odot}$. We find $\Delta_{\text{max}}(\log n_{\text{H}}) = 0.73$ and $\Delta_{\text{max}}(\log Z) = 0.1$ dex for left-hand panel and $\Delta_{\text{max}}(\log n_{\text{H}}) = 0.47$ and $\Delta_{\text{max}}(\log Z) = 0.02$ dex for right-hand panel indicating inferred n_{H} and Z show less variation at higher true n_{H} . Given negligibly small deviation in inferred Z from its true value, we can safely say that estimates of Z are robust for warm-hot absorbers.

for our test case shown in Fig. 8 the set of five ions used for the inference has Ne VIII.

In order to check the dependence of different values of true n_{H} and Z used in mock warm-hot absorber on the the values of Δ_{max} , as in the case of photoionized absorber we redo the analysis for nine combinations of true n_{H} and Z where we change n_{H} from 10^{-5} to 10^{-3} cm^{-3} and Z from $10^{-2} Z_{\odot}$ to $1 Z_{\odot}$. Results for two such combinations are shown in Fig. 10 where the n_{H} and Z inference used 83 sets of eight ions which include ion Ne VIII. There is more scatter at the inferred values of n_{H} and Z for lower values of true n_{H} , as can be seen by comparing left and right-hand panel of Fig. 10.

However, note that warm-hot absorbers show significantly less variation in the inferred Z as compared to the photoionized absorbers.

We find that for the same true n_{H} and Z there is a small change in $\Delta_{\text{max}}(\log n_{\text{H}})$ values of the order of 0.1 dex if we use different true

UV background models in our mock warm-hot absorbers. Therefore, we repeat the analysis by changing the true UV background models and then take the mean of the Δ_{max} values from all nine true UV background models. Final values of $\Delta_{\text{max}}(\log n_{\text{H}})$ and $\Delta_{\text{max}}(\log Z)$ are given in Table 2 and also shown in Fig. 11 as error-bars on the true values of n_{H} and Z . The blue error-bars show the extend of Δ_{max} when we include Ne VIII in the ions used for inference and cyan error-bars when we do not include Ne VIII.

The annotated values in the figure are the $\Delta_{\text{max}}(\log n_{\text{H}})/2$ and $\Delta_{\text{max}}(\log Z)/2$ which are equivalent to being systematic uncertainties on the $\log n_{\text{H}}$ and $\log Z$ arising from uncertain UV background. When we do not use Ne VIII then inferred values of n_{H} do not show any dependence on the true n_{H} values and for all the cases the $\Delta_{\text{max}}(\log n_{\text{H}}) \sim 0.86$. In this case, there is more scatter in the inferred Z at true $n_{\text{H}} = 10^{-5} \text{ cm}^{-3}$ giving rise to $\Delta_{\text{max}}(\log Z) = 0.3$ dex as compared to 0.1 dex when Ne VIII is included in the inference.

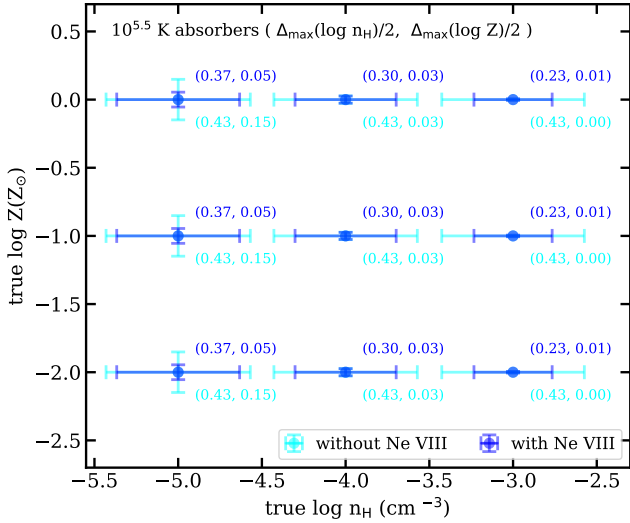


Figure 11. The grid of true n_{H} and Z where the extent of error-bars show the uncertainty (Δ_{max} values) on the inferred n_{H} (horizontal error-bars) and Z (vertical error-bars) for warm-hot absorbers at $T = 10^{5.5}$ K from all nine UV background models. The annotated values in the brackets show the $\Delta_{\text{max}}(\log n_{\text{H}})/2$ and $\Delta_{\text{max}}(\log Z)/2$ which can be quoted as systematic uncertainty on the inferred values of n_{H} and Z using CGM observations. Blue and cyan error-bars and annotated values indicate results when we include Ne VIII column density for the inference and when we do not, respectively. The values for former are also given in Table 2.

Whereas, for true $n_{\text{H}} > 10^{-5} \text{ cm}^{-3}$, the $\Delta_{\text{max}}(\log Z)$ is negligibly small and does not depend on inclusion or exclusion of Ne VIII. With increasing true n_{H} , $\Delta_{\text{max}}(\log Z)$ reduces rapidly and approaches to zero at $n_{\text{H}} \sim 10^{-3} \text{ cm}^{-3}$. Therefore one can safely say that for warm-hot absorbers at $n_{\text{H}} \gtrsim 10^{-4} \text{ cm}^{-3}$ inferred metallicity is robustly estimated. Fig. 11 shows that $\Delta_{\text{max}}(\log n_{\text{H}})$ values do not depend on the true Z , whereas $\Delta_{\text{max}}(\log n_{\text{H}})$ changes from 0.74 to 0.46 dex when true n_{H} changes from 10^{-5} to 10^{-3} cm^{-3} (when we include Ne VIII in the inference). Similar to the case of photoionized absorber, we find that both n_{H} and Z are better constrained for gas at high densities.

Overall, for the warm-hot absorbers at $T = 10^{5.5}$ K, Z is robustly estimated (within 0.05 dex) for gas with density $\geq 10^{-4} \text{ cm}^{-3}$ whereas the inferred n_{H} can be uncertain up to a value of $\Delta_{\text{max}}(\log n_{\text{H}})$ ranging from 0.46 to 0.74 dex for the gas with density 10^{-3} to 10^{-5} cm^{-3} . However, excluding Ne VIII from the analysis can increase the $\Delta_{\text{max}}(\log n_{\text{H}})$ up to 0.86 dex. Table 2 provides values of Δ_{max} for different true n_{H} and Z for all nine UV background (shown in Fig 11) as well as for only seven KS19 UV background models. However, note that our results assume that observers know the true temperature of the gas and therefore the quoted uncertainties are only related to the varying models of UV background.

4.3 Shape and Normalization of the UV Background

Here, in order to understand the trend in the inferred n_{H} and Z as well as to find out how much $\Delta_{\text{max}}(\log n_{\text{H}})$ and $\Delta_{\text{max}}(\log Z)$ is contributed by the change in UV background shapes as compared to its normalization (or Γ_{HI}), we normalize all UV background models to have same Γ_{HI} value and repeat the analysis for the test case. This normalization is performed by scaling all UV background models to have same Γ_{HI} as in Q18 KS19 model. In Fig. 12, we show these

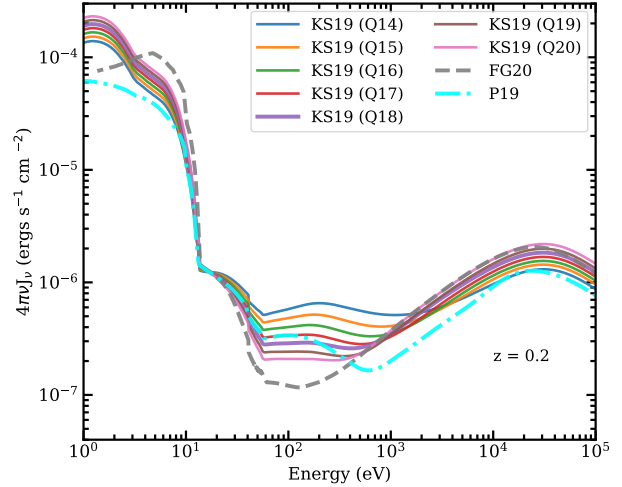


Figure 12. Rescaled UV background models at $z = 0.2$. Here, every UV background spectrum has been normalised so that all of them have same Γ_{HI} as in Q18 model of KS19. Legends are the same as given in Fig. 1.

normalized UV background spectra at $z = 0.2$. Because of the simple scaling to keep Γ_{HI} same, all models are close to each other at $E \sim 13.6 \text{ eV}$ but they differ at high and low energies (compare Fig. 1 and 12). We use these Γ_{HI} normalized UV background models and repeat our analysis for the test case (shown in Fig. 4 and 8) for both photoionized and hybrid warm-hot mock absorbers generated using Q18 KS19 as a true UV background.

Results of this exercise are summarized in the Fig 13. We also show the previous results (from Fig. 8 and 4) obtained using original UV background models for comparison. We get the same inferred Z for both photoionized and hybrid absorbers (right hand panels in Fig 13) as in original UV background models. It clearly illustrates that the main reason behind the variation in the inferred metallicity is the change in shape of UV background models whereas the scaling of UVB has no effect on the metallicity. Shape of a UV background model decides the relative values of photoionization rates for all metal species which are independent of the scaling of UV background. The scaled UV background uniformly scales all metal-ion column densities, therefore inferred Z does not change with scaling of UV background. However, in order to reproduce these uniformly scaled metal ion column densities, inferred n_{H} gets scaled with same factor as UV background. We see it in the inferred n_{H} for re-scaled UV background models (blue points in Fig. 13) as compared to the one with original UV background models (yellow points in Fig. 13) where the ratio of new to original n_{H} is equal to the UV background scaling factor. Such a scaling of n_{H} with UV background arises because total hydrogen column density N_{H} is proportional to the $\Gamma_{\text{HI}}/n_{\text{H}}$ for low density IGM and CGM clouds.⁵ Since inferred Z is independent of UV background scaling, to obtain the observed column densities of metal ions, N_{H} should be same. Therefore, n_{H} scales with the Γ_{HI} i.e., with the scaling factor of the UV background. In other words, this scaling of n_{H} is a result of preserving ionization parameter for all ions since scaling UV

⁵ It can be understood in terms of photoionization equilibrium for hydrogen gas where $\Gamma_{\text{HI}} \propto (1 - x_{\text{HI}})^2 n_{\text{H}} N_{\text{H}}$ ignoring small temperature dependence of hydrogen recombination coefficient for a fixed value of N_{H} . For the low density IGM and CGM gas, the neutral fraction $x_{\text{HI}} = n_{\text{HI}}/n_{\text{H}} \ll 1$ implies $N_{\text{H}} \propto \Gamma_{\text{HI}}/n_{\text{H}}$.

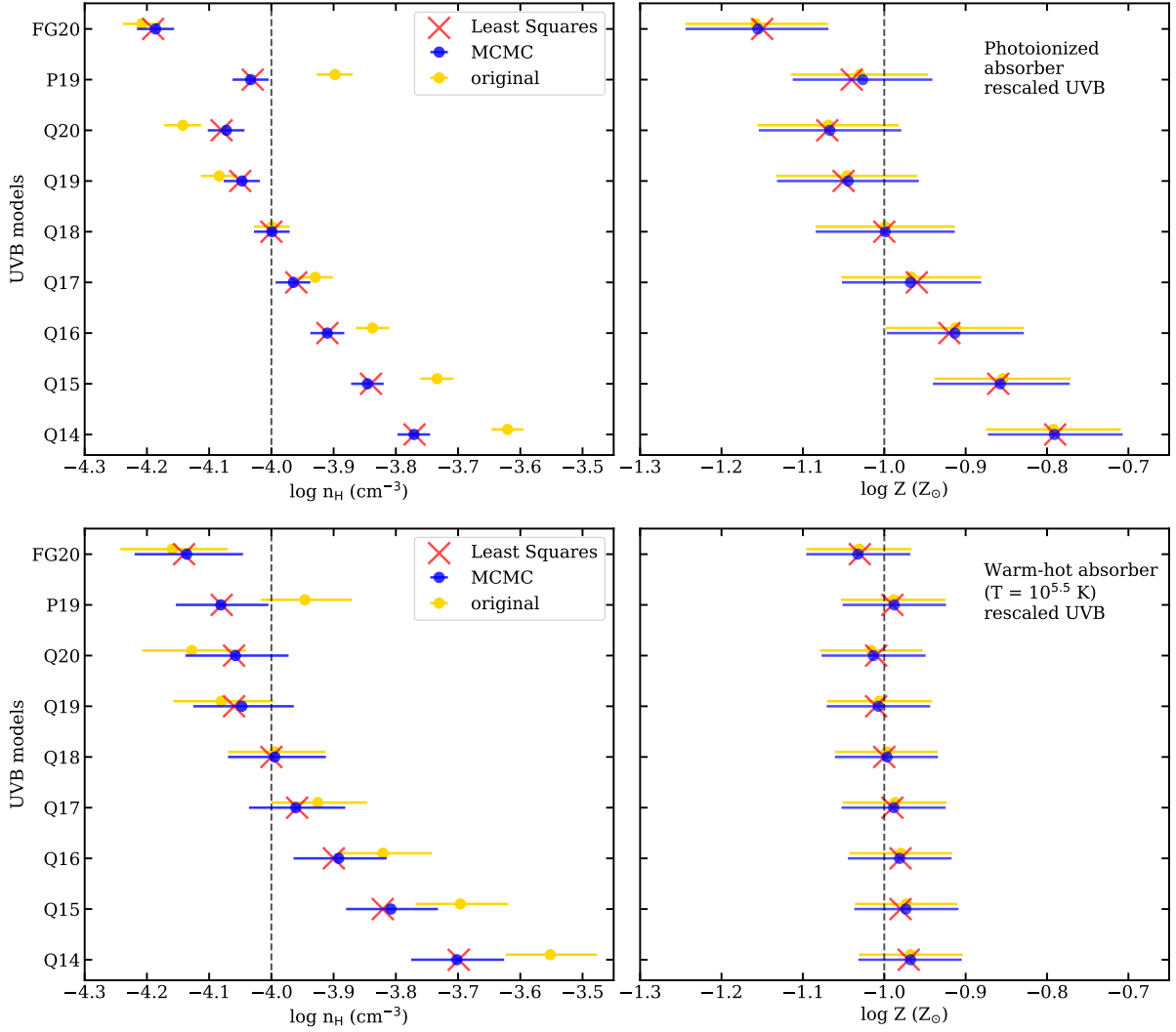


Figure 13. Inferred values of n_{H} (cm^{-3} ; left-hand panel) and Z (Z_{\odot} ; right-hand panel) for re-scaled UV background models (labeled on y-axis; see Fig. 12) that have same Γ_{HI} values. Results for the photoionized (top panels) and the warm-hot ($T = 10^{5.5}$ K) mock observations are shown along with the previous results (with yellow data points) obtained for original UV background (presented in Fig. 4 and 8). Models Q14-Q20 are from KS19. The blue circles with horizontal error-bars show the result from the Bayesian MCMC method (median with 16 and 84 percentile values of posterior PDF; see Fig. A1 for few illustrations) while the red crosses shows the result of least square minimization method. Vertical dashed lines indicate the true values from toy observations obtained using Q18 KS19 UV background model. The same results in metallicity for original and scaled UV background models show that the metallicity is independent of scaling and depends only on the shape of the UV background. As expected, for both photoionized and hybrid models, the inferred n_{H} (blue points) changes by same scaling factors used for UV background from the previous inferred values (yellow point). For photoionized models, total difference in the inferred n_{H} arising only from change in shape of UV background models $\Delta_{\text{max}}(\log n_{\text{H}}) = 0.4$ and metallicity change is same as original UV background models $\Delta_{\text{max}}(\log Z) = 0.66$. For warm-hot absorber at $T = 10^{5.5}$ K the total variation in density $\Delta_{\text{max}}(\log n_{\text{H}}) = 0.44$ as compared to original 0.56 dex.

background uniformly scales n_i by same amount for all metal ions. Therefore, to reproduce abundance pattern of all ions the inferred n_{H} scales with the same UV background scaling.

For such scaled UV backgrounds, we see reduced variation in the inferred n_{H} values for both photoionized and warm-hot absorbers as compared to the values obtained with original UV background models. In case of photoionized models, we find $\Delta_{\text{max}}(\log n_{\text{H}}) = 0.4$ dex as compared to previous (with un-normalised original UV background) value of 0.66 dex, and in case of warm-hot gas the $\Delta_{\text{max}}(\log n_{\text{H}}) = 0.44$ dex as compared to previous value of 0.56 dex. The still significant values of $\Delta_{\text{max}}(\log n_{\text{H}}) \sim 0.4$ dex despite the fact that Γ_{HI} is same for all UV background models, suggest that *the inferred n_{H} depends both on the normalization and shape of*

the UV background. Here, the variation $\Delta_{\text{max}}(\log n_{\text{H}}) \sim 0.4$ dex is arising due to change in shape of the UV background models. This is mainly due to jointly constraining the metallicity and density. The relative change in metal column densities arising due to shape of UV background demands different density of the gas. In order to naively understand the trend, consider following argument; for a given value of n_{H} a harder (softer) UV background will result into lower (higher) column densities of metal ions therefore the inference will prefer higher (lower) density of gas than n_{H} so there is more (less) self shielding to match (higher) lower values of observed metal column densities. Note that, the variation $\Delta_{\text{max}}(\log n_{\text{H}})$ is too large to be explained with only ionization parameter of hydrogen.

To understand the trend in inferred n_{H} and Z , it is better to have

UV background models that vary minimum number of parameters, as in the case of seven models of **KS19**. For example, even though the **P19** model use $\alpha = 1.7$ as quasar SED, the UV background spectrum is not same as Q17 model of **KS19** or **FG20** which also use $\alpha = 1.7$. It is because other parameters such as the quasar emissivity at 13.6 eV or the distribution of H I gas in IGM are different, which changes the shape of the UV background spectrum. We find that the spectrum of **P19** at $E < 50$ eV lies somewhere in between Q18 and Q19 models. This explains trend in the inferred metallicity for **P19** UV background (e.g., in Fig. 5, 6 and 10). The Γ_{HI} for **P19** is higher than the Q18 model (at $z = 0.2$; see Fig. 2) which results into higher inferred n_{H} than for Q18 (e.g., in Fig. 5, 6). Note that the inferred n_{H} does depend on both spectrum and the normalization, therefore when we normalize **P19** to same Γ_{HI} of Q18 model, we infer the lower n_{H} values, as shown in Fig. 13.

4.4 Other Uncertainties and Caveats

We recommend quoting $\pm\Delta_{\text{max}}(\log n_{\text{H}})/2$ and $\pm\Delta_{\text{max}}(\log Z)/2$ from Fig. B1 for clouds with different N_{HI} and Fig. 11 for hybrid absorbers as a systematic uncertainty on the inferred n_{H} and Z arising from uncertain UV background models. For example, in case of $N_{\text{HI}} \sim 10^{15} \text{ cm}^{-2}$ absorber if the inferred $\log n_{\text{H}}(\text{cm}^{-3})$ and $\log Z/Z_{\odot}$ from some CGM observations assuming photoionization equilibrium results in to values of -4.8 and -1.2 , one can read off the $\Delta_{\text{max}}(\log n_{\text{H}})$ and $\Delta_{\text{max}}(\log Z)$ from its closest point ($\log n_{\text{H}}, \log Z$) $\equiv (-5, -1)$ in Fig 7 (or Table 1) and quote ± 0.4 and ± 0.23 as a systematic uncertainty on $\log n_{\text{H}}$ and $\log Z$, respectively. We checked the redshift evolution of the $\Delta_{\text{max}}(\log n_{\text{H}})$ and $\Delta_{\text{max}}(\log Z)$ for both photoionized and warm-hot absorber and found no significant change in the values at $z < 1.5$.

Although we recommend using $\pm\Delta_{\text{max}}(\log n_{\text{H}})/2$ and $\pm\Delta_{\text{max}}(\log Z)/2$ as a systematic uncertainty, we caution readers that it need not be symmetric. For example if one uses **FG20** background model to infer the n_{H} then the uncertainty should be $+\Delta_{\text{max}}(\log n_{\text{H}})$ and -0 , given the fact that all other models, being harder than **FG20**, infer higher n_{H} . Moreover, note that the uncertainties obtained here are under the assumption of simplest possible CGM absorbers with uniform density and metallicity. Complex multi-phase configuration with non-equilibrium conditions may require their own analysis. However note that, as long as a part of cloud assumed to have uniform density and metallicity irradiated with a UV background, uncertainties arising from UV background will be similar to the one presented here. For example, even for multi-phase gas as invoked in many studies (e.g. **Pachat et al. 2016, 2017; Nateghi et al. 2021; Haislmaier et al. 2020**), each phase will have similar uncertainty from UV background. Even with innovative techniques to models individual cloudlets as presented in **Sameer et al. (2021)**, each cloudlet and its phase will suffer with same uncertainty from UV background as long as a preferred UV background model is fixed for the inference.

In real observations, fitting uncertainties on the n_{H} and Z (say Δ_{fit}) can be obtained from various fitting methods used to find solution for n_{H} and Z , such as the confidence intervals from our Bayesian MCMC approach. These uncertainties depend on the column density measurement errors of ions used for the inference. In the calculations presented here, we assumed a fixed value of N_{HI} and used it as a stopping criteria for cloudy models, whereas observations will have measurement errors ΔN_{HI} , for example, from Voigt-profile fitting of H I absorption lines. To find out how much ΔN_{HI} contributes to the error budget on inferred n_{H} and Z we ran cloudy models with different N_{HI} as a stopping criteria and found that the inferred

Table 1. Maximum variation in n_{H} and Z for photoionized absorber with $N_{\text{HI}} = 10^{15} \text{ cm}^{-2}$ (from Fig. 7), refer to Fig. B1 for different N_{HI} .

| True $\log n_{\text{H}}$ (cm^{-3}) | True $\log Z$ (Z_{\odot}) | Δ_{max} ($\log n_{\text{H}}$) all UVB | Δ_{max} ($\log Z$) all UVB | Δ_{max} ($\log n_{\text{H}}$) KS19 | Δ_{max} ($\log Z$) KS19 |
|---|-------------------------------|---|--|--|---|
| -5 | -2 | 0.79 | 0.44 | 0.69 | 0.36 |
| -5 | -1 | 0.80 | 0.47 | 0.69 | 0.36 |
| -5 | 0 | 0.75 | 0.57 | 0.67 | 0.42 |
| -4 | -2 | 0.72 | 0.57 | 0.61 | 0.41 |
| -4 | -1 | 0.72 | 0.57 | 0.60 | 0.41 |
| -4 | 0 | 0.65 | 0.56 | 0.55 | 0.40 |
| -3 | -2 | 0.54 | 0.35 | 0.49 | 0.24 |
| -3 | -1 | 0.54 | 0.35 | 0.49 | 0.24 |
| -3 | 0 | 0.52 | 0.36 | 0.47 | 0.25 |

Note: Here, ‘all UVB’ refers to all nine models of UV background while ‘KS19’ refers to seven models of **KS19**.

Table 2. Maximum variation in n_{H} and Z for warm hot absorber at $T = 10^{5.5}$ K including Ne VIII (see Fig. 11)

| True $\log n_{\text{H}}$ (cm^{-3}) | True $\log Z$ (Z_{\odot}) | Δ_{max} ($\log n_{\text{H}}$) all UVB | Δ_{max} ($\log Z$) all UVB | Δ_{max} ($\log n_{\text{H}}$) KS19 | Δ_{max} ($\log Z$) KS19 |
|---|-------------------------------|---|--|--|---|
| -5 | -2 | 0.73 | 0.11 | 0.67 | 0.05 |
| -5 | -1 | 0.73 | 0.11 | 0.67 | 0.05 |
| -5 | 0 | 0.73 | 0.11 | 0.67 | 0.05 |
| -4 | -2 | 0.60 | 0.05 | 0.57 | 0.04 |
| -4 | -1 | 0.60 | 0.05 | 0.57 | 0.04 |
| -4 | 0 | 0.60 | 0.05 | 0.57 | 0.04 |
| -3 | -2 | 0.47 | 0.01 | 0.47 | 0.01 |
| -3 | -1 | 0.47 | 0.01 | 0.47 | 0.01 |
| -3 | 0 | 0.47 | 0.01 | 0.47 | 0.01 |

Note: Here, ‘all UVB’ refers to all nine models of UV background while ‘KS19’ refers to seven models of **KS19**.

n_{H} is independent of N_{HI} values but the inferred Z scales linearly with the change in N_{HI} . This is the reason for the correlation seen in the 2D posteriors for photoionized gas (as in Fig. A1 and right-hand side of Fig. 3). Therefore, total error on n_{H} has to be the sum of systematic error from UV background models ($\Delta_{\text{max}}(\log n_{\text{H}})/2$) and Δ_{fit} (i.e here, confidence intervals from Bayesian MCMC fits). Whereas, error on inferred Z should include $\Delta_{\text{max}}(\log Z)/2$, Δ_{fit} and ΔN_{HI} . Therefore, as long as the $\Delta N_{\text{HI}} \gg \Delta_{\text{max}}(\log Z)/2$, systematic uncertainty from UV background may not play an important role in total error budget of inferred Z . Note that we are only discussing the errors on n_{H} and Z arising from UV background and their relation to the observed errors on N_{HI} . There are other potential effects such as poorly known gas temperature that will have its own uncertainty, quantifying which is beyond the scope of this paper.

5 SUMMARY AND CONCLUSION

We studied the effect of using different UV background models on the inferred density n_{H} and metallicity Z of CGM absorbers. We chose nine viable UV background models from most recent and updated studies (see Fig. 1) which include seven models generated

with varying quasar SED from [KS19](#) and two models from [FG20](#) and [P19](#).

First, using `CLOUDY` software for ionization modelling, we created two sets of toy models one for photoionized absorber and other for collisionally ionized warm-hot absorber. We irradiated these absorbers with a fiducial UV background model and noted down the model column densities of many metal ions commonly observed in the CGM. We treat a set of those metal-ion column densities along with N_{HI} as our toy observations. Then we use these toy observations to infer the n_{H} and Z using different UV background models.

We use two methods to jointly infer the n_{H} and Z from such toy observations, the maximum likelihood estimate using the Bayesian MCMC method and by minimizing the least square difference in the model and observed (from toy models) column densities. We show that both methods provide identical results. To quantify the variation in the n_{H} and Z , we define total variation $\Delta_{\text{max}}(\log n_{\text{H}})$ and $\Delta_{\text{max}}(\log Z)$ which is the maximum difference in the inferred median values of n_{H} and Z obtained using large set of mock observations assuming all nine UV background models.

For photoionized CGM absorbers, we find that the $\Delta_{\text{max}}(\log n_{\text{H}})$ ranges from 0.5 to 0.8 dex (a factor of 3.2 to 6.3 difference) whereas $\Delta_{\text{max}}(\log Z)$ ranges from 0.2 to 0.6 dex (a factor of 1.6 to 4) difference for CGM clouds having density 10^{-3} to 10^{-5} cm^{-3} and hydrogen column N_{HI} ranging from 10^{14} to 10^{19} cm^{-2} . The n_{H} and Z dependent values of Δ_{max} are shown in [Fig. B1](#).

For collisionally ionized CGM absorbers at $T = 10^{5.5}$ K, we find that including Ne VIII column density in the inference provides better results that are closer to the true values ([Fig. 5](#)). Interestingly, we find that the inferred Z is always robustly estimated (within ~ 0.1 dex). However, $\Delta_{\text{max}}(\log n_{\text{H}})$ ranges from 0.47 to 0.73 dex (a factor of 3 to 5.4) difference for CGM clouds having density 10^{-3} to 10^{-5} cm^{-3} . If Ne VIII is not included in the inference, the $\Delta_{\text{max}}(\log n_{\text{H}})$ and $\Delta_{\text{max}}(\log Z)$ further increases by ~ 0.2 dex. The n_{H} and Z dependent values of Δ_{max} with and without Ne VIII for warm-hot absorber are shown in [Fig. 11](#) and tabulated in [Table 2](#).

We recommend quoting $\pm\Delta_{\text{max}}(\log n_{\text{H}})/2$ and $\pm\Delta_{\text{max}}(\log Z)/2$ from [Fig. B1](#) and [Fig. 11](#) as a systematic uncertainty on the inferred n_{H} and Z arising from uncertain UV background models for photoionized and warm-hot absorber, respectively. For a case of $N_{\text{HI}} = 10^{15}$ cm^{-2} absorber, we also provide these Δ_{max} values in [Table 1](#) and [2](#) along with the one obtained only for seven UV background models of ([KS19](#)) where different UV background were obtained by changing only one parameter i.e shape of quasar SED. Note that these results are valid for the IGM and CGM absorbers having density in the range $n_{\text{H}} < 10^{-2}$ cm^{-3} . At very high densities ionization fraction for hydrogen and metals may drop sharply due to self shielding and then the inferred values may become less sensitive to the incident UV background.

To study which factor, the shape or the amplitude (normalization) of the UV background, is important for the obtained variation in the n_{H} and Z , we ran more `CLOUDY` models with modified UV background by scaling all nine UV backgrounds to have same H I photoionization rates (Γ_{HI}) as in fiducial Q18 [KS19](#) UV background model. These re-scaled backgrounds (see [Fig 12](#)) differ only in the relative shapes. From these models we find that the inferred metallicity for photoionized absorbers only depends on the shape of the UV background and it is independent of the normalization, whereas inferred n_{H} depends on both the shape and normalization of UV background. We find, *harder (softer) UV background implies high (low) n_{H} and Z .*

The inferred density and metallicity is directly related to the line-of-sight thickness of CGM clouds and their mass. Thus, the

large variation in these parameters suggests that we need to be cautious while interpreting the results of CGM studies and ionization models using just one UV background model. On the other hand, this demands more constraining observations of input parameters used in synthesis of UV background models, especially the ones that determine the shape of the UV background, such as the intrinsic SED of quasars at ionizing energies. This would allow the future UV background models to provide a more precise picture of the CGM.

ACKNOWLEDGEMENTS

AA thanks Robert Antonucci for hosting him at the University of California, Santa Barbara and helpful discussions on the topic. AA acknowledges financial support from the Kishore Vaigyanik Protsahan Yojana (KVPY) Fellowship for undergraduates by the Department of Science and Technology, Government of India. VK is supported through the INSPIRE Faculty Award (No. DST/INSPIRE/04/2019/001580) of the Department of Science and Technology (DST), India. Authors would also like to thank the discussions and suggestions in the KITP Halo21 workshop, supported in part by the National Science Foundation under Grant No. NSF PHY-1748958. Authors would also like to thank Abhisek Mohapatra for his feedback, suggestions and comments on the paper. Lastly, the authors would like to thank the anonymous referee for their suggestions and comments which helped in improving this paper significantly.

DATA AVAILABILITY

No observational data was used for this project. The outputs for both the photoionized and warm-hot absorber models for all UV backgrounds can be made publicly available on request.

REFERENCES

- Bordoloi R., et al., 2014, [ApJ](#), **796**, 136
 Burchett J. N., et al., 2019, [ApJ](#), **877**, L20
 Caruso D., Haardt F., Fumagalli M., Cantalupo S., 2019, [MNRAS](#), **482**, 2833
 Chen H.-W., Johnson S. D., Zahedy F. S., Rauch M., Mulchaey J. S., 2017, [ApJ](#), **842**, L19
 Chen H.-W., et al., 2020, [MNRAS](#), **497**, 498
 Churchill C. W., Vander Vliet J. R., Trujillo-Gomez S., Kacprzak G. G., Klypin A., 2015, [ApJ](#), **802**, 10
 Cooke R., Pettini M., Steidel C. C., Rudie G. C., Nissen P. E., 2011, [MNRAS](#), **417**, 1534
 Danforth C. W., et al., 2016, [ApJ](#), **817**, 111
 Faucher-Giguère C.-A., 2020, [MNRAS](#), **493**, 1614
 Faucher-Giguère C.-A., Lidz A., Zaldarriaga M., Hernquist L., 2009, [ApJ](#), **703**, 1416
 Ferland G. J., Korista K. T., Verner D. A., Ferguson J. W., Kingdon J. B., Verner E. M., 1998, [PASP](#), **110**, 761
 Ferland G. J., et al., 2017, [Rev. Mex. Astron. Astrofis.](#), **53**, 385
 Foreman-Mackey D., Hogg D. W., Lang D., Goodman J., 2013, [PASP](#), **125**, 306
 Gaikwad P., Khaire V., Choudhury T. R., Srianand R., 2017a, [MNRAS](#), **466**, 838
 Gaikwad P., Srianand R., Choudhury T. R., Khaire V., 2017b, [MNRAS](#), **467**, 3172
 Grevesse N., Asplund M., Sauval A. J., Scott P., 2010, [Ap&SS](#), **328**, 179
 Haardt F., Madau P., 1996, [ApJ](#), **461**, 20
 Haardt F., Madau P., 2012, [ApJ](#), **746**, 125

- Haislmaier K. J., Tripp T. M., Katz N., Prochaska J. X., Burchett J. N., O'Meara J. M., Werk J. K., 2020, *MNRAS*,
- Hummels C. B., Bryan G. L., Smith B. D., Turk M. J., 2013, *MNRAS*, **430**, 1548
- Hummels C. B., et al., 2019, *ApJ*, **882**, 156
- Hussain T., Muzahid S., Narayanan A., Srianand R., Wakker B. P., Charlton J. C., Pathak A., 2015, *MNRAS*, **446**, 2444
- Hussain T., Khaire V., Srianand R., Muzahid S., Pathak A., 2017, *MNRAS*, **466**, 3133
- Khaire V., 2017, *MNRAS*, **471**, 255
- Khaire V., Srianand R., 2013, *MNRAS*, **431**, L53
- Khaire V., Srianand R., 2015, *MNRAS*, **451**, L30
- Khaire V., Srianand R., 2019, *MNRAS*, **484**, 4174
- Khaire V., et al., 2019, *MNRAS*, **486**, 769
- Kollmeier J. A., et al., 2014, *ApJ*, **789**, L32
- Kulkarni G., Worseck G., Hennawi J. F., 2018, preprint, ([arXiv:1807.09774](https://arxiv.org/abs/1807.09774))
- Lehner N., et al., 2013, *The Astrophysical Journal*, **770**, 138
- Lusso E., Worseck G., Hennawi J. F., Prochaska J. X., Vignali C., Stern J., O'Meara J. M., 2015, *MNRAS*, **449**, 4204
- Lusso E., Fumagalli M., Rafelski M., Neeleman M., Prochaska J. X., Hennawi J. F., O'Meara J. M. T., 2018, *ApJ*, **860**, 41
- Miralda-Escude J., Ostriker J. P., 1990, *ApJ*, **350**, 1
- Mohapatra A., Srianand R., Khaire V., Pradhan A. C., 2019, *MNRAS*, **484**, 5028
- Mohapatra A., Srianand R., Pradhan A. C., 2021, *MNRAS*, **501**, 5424
- Narayanan A., Wakker B. P., Savage B. D., 2009, *ApJ*, **703**, 74
- Nateghi H., Kacprzak G. G., Nielsen N. M., Muzahid S., Churchill C. W., Pointon S. K., Charlton J. C., 2021, *MNRAS*, **500**, 3987
- Nelson D., et al., 2020, *MNRAS*, **498**, 2391
- Oppenheimer B. D., Schaye J., Crain R. A., Werk J. K., Richings A. J., 2018, *MNRAS*, **481**, 835
- Pachat S., Narayanan A., Muzahid S., Khaire V., Srianand R., Wakker B. P., Savage B. D., 2016, *MNRAS*, **458**, 733
- Pachat S., Narayanan A., Khaire V., Savage B. D., Muzahid S., Wakker B. P., 2017, *MNRAS*, **471**, 792
- Peeples M. S., et al., 2019, *ApJ*, **873**, 129
- Pettini M., Zych B. J., Steidel C. C., Chaffee F. H., 2008, *MNRAS*, **385**, 2011
- Planck Collaboration et al., 2018, preprint, ([arXiv:1807.06209](https://arxiv.org/abs/1807.06209))
- Prochaska J. X., et al., 2017, *ApJ*, **837**, 169
- Puchwein E., Haardt F., Haehnelt M. G., Madau P., 2019, *MNRAS*, **485**, 47
- Sameer et al., 2021, *MNRAS*, **501**, 2112
- Savage B. D., Kim T.-S., Wakker B. P., Keeney B., Shull J. M., Stocke J. T., Green J. C., 2014, *ApJS*, **212**, 8
- Shull J. M., Roberts D., Giroux M. L., Penton S. V., Fardal M. A., 1999, *AJ*, **118**, 1450
- Shull J. M., Stevans M., Danforth C. W., 2012a, *ApJ*, **752**, 162
- Shull J. M., Smith B. D., Danforth C. W., 2012b, *ApJ*, **759**, 23
- Shull J. M., Danforth C. W., Tilton E. M., 2014, *ApJ*, **796**, 49
- Shull J. M., Moloney J., Danforth C. W., Tilton E. M., 2015, *ApJ*, **811**, 3
- Stevans M. L., Shull J. M., Danforth C. W., Tilton E. M., 2014, *ApJ*, **794**, 75
- Stocke J. T., Keeney B. A., Danforth C. W., Shull J. M., Froning C. S., Green J. C., Penton S. V., Savage B. D., 2013a, *ApJ*, **763**, 148
- Stocke J. T., Keeney B. A., Danforth C. W., Shull J. M., Froning C. S., Green J. C., Penton S. V., Savage B. D., 2013b, *ApJ*, **763**, 148
- Tilton E. M., Stevans M. L., Shull J. M., Danforth C. W., 2016, *ApJ*, **817**, 56
- Tripp T. M., Sembach K. R., Bowen D. V., Savage B. D., Jenkins E. B., Lehner N., Richter P., 2008, *ApJS*, **177**, 39
- Tumlinson J., et al., 2013, *ApJ*, **777**, 59
- Tumlinson J., Peeples M. S., Werk J. K., 2017, *ARA&A*, **55**, 389
- Wotta C. B., Lehner N., Howk J. C., O'Meara J. M., Oppenheimer B. D., Cooksey K. L., 2019, *The Astrophysical Journal*, **872**, 81
- van de Voort F., Springel V., Mandelker N., van den Bosch F. C., Pakmor R., 2019, *MNRAS*, **482**, L85

APPENDIX A: POSTERIOR PDFS FOR FEW EXAMPLE CASES**APPENDIX B: RESULTS ON VARYING OPTICAL THICKNESS OF CLOUD**

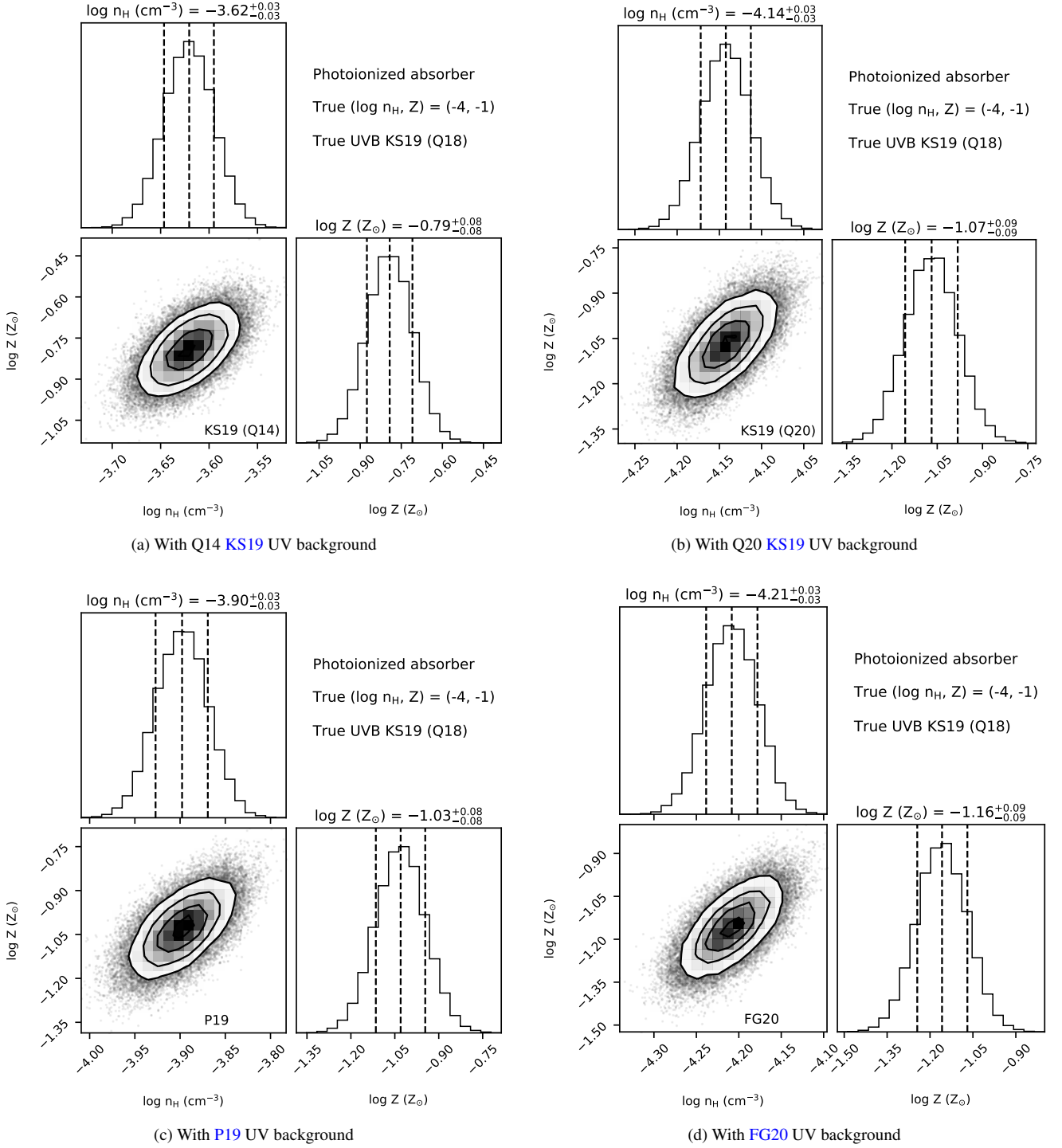


Figure A1. Some example posterior PDFs similar to the one shown in Fig. 3 but the inference is performed assuming different models. The panel (a) and (b) are obtained by using two Q14 and Q20 models of the UV background while panel (c) and (d) are obtained by using P19 and FG20 models of the UV background. Note that the mock observations are obtained by using Q18 KS19 UV background models having true values $\log n_{\text{H}}(\text{cm}^{-3}) = -4$ and $\log Z(Z_{\odot}) = -1$.

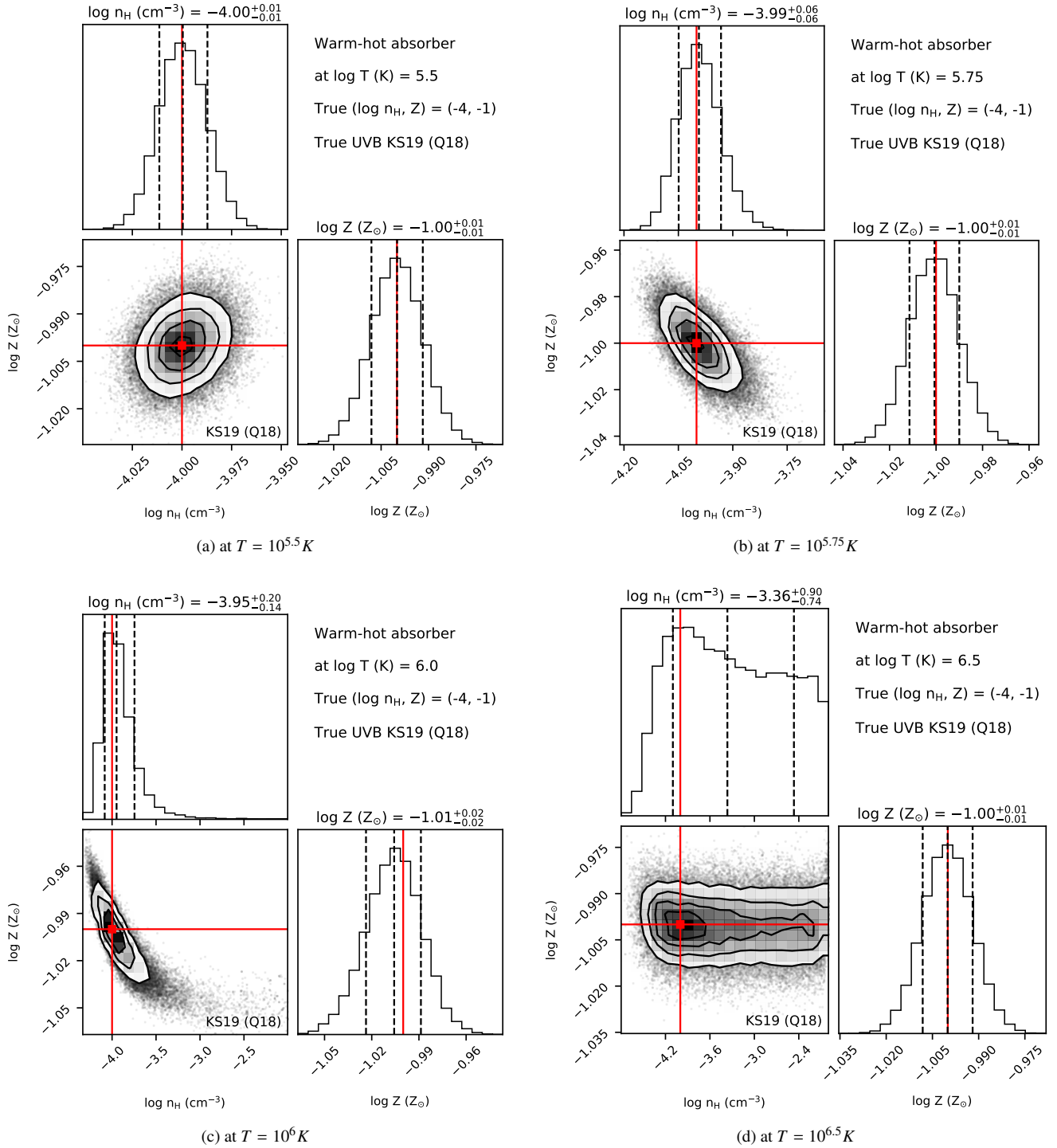


Figure A2. Example inference tests for warm-hot absorbers at different temperature where red lines indicate the true values. For these tests, we used very small errors on the column densities of metal ions (< 0.1 dex) so that posteriors are well behaved upto $T = 10^6 K$. As we increase temperature, density becomes more unconstrained, however metallicity always remains well constrained.

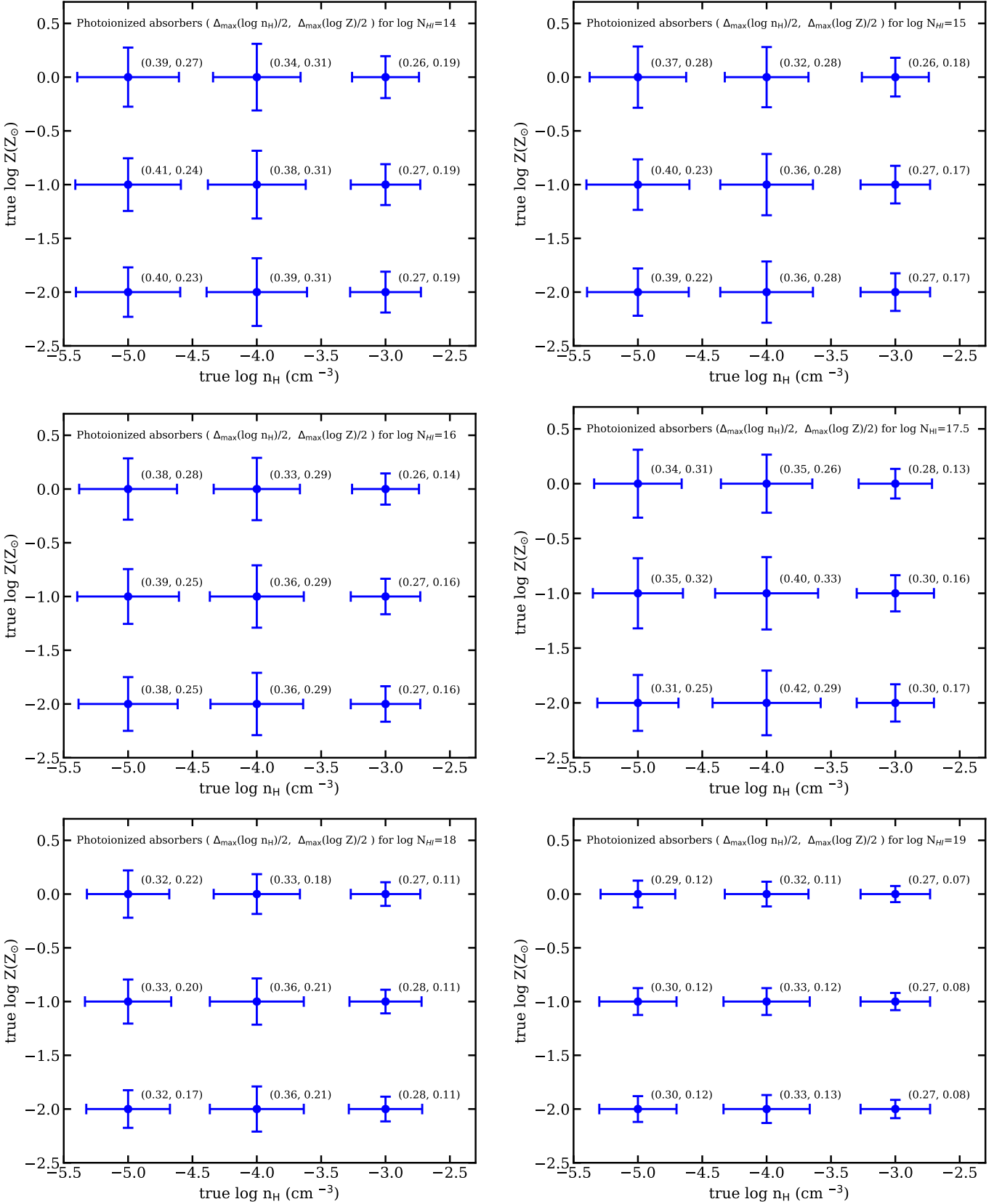


Figure B1. Results for a range of different H I column densities $\log N_{\text{HI}} = 10^{14} \text{ cm}^{-2}$ to $\log N_{\text{HI}} = 10^{19} \text{ cm}^{-2}$. Note that optical thickness of the cloud does not seem to have a significant effect on the results. Note that the result using a stopping column density of $\log N_{\text{HI}} = 10^{15} \text{ cm}^{-2}$ are shown in figure 7.